Antibody-based immunotherapy targeting FAM19A5 reverses synaptic loss and improves cognitive function in Alzheimer's disease.

Authors: Han-Byul Kim[1†], Sangjin Yoo[1†], Hoyun Kwak[1†], Shi-Xun Ma[1†], Ryunhee Kim[1], Minhyeok Lee[1], Nui Ha[1], Soonil Pyo[1], Soon-Gu Kwon[1], Eun-Ho Cho[1], Sang-Myeong Lee[1], Juwon Jang[1], Wonkyum Kim[1,2], Hae-Chul Park[3], Minkyung Baek[4], Yosub Park[1], Ji-Young Park[5], Jin-Woo Park[6,7], Sun Wook Hwang[8], Jong-Ik Hwang[8], Jae Young Seong[1, 8, *]

Affiliations:

[1]Neuracle Science Co., Ltd., Seoul 02841, Republic of Korea
[2]Department of Biological Sciences, Korea Advanced Institute of Science and Technology, 291 Daehak-ro, Yuseong-gu, Daejeon, 34141, Republic of Korea
[3]Department of Biomedical Sciences, Graduate School of Medicine, Korea University, Ansan, Gyeonggido 425-707, Republic of Korea
[4]School of Biological Sciences, Seoul National University, Seoul 08826, Republic of Korea
[5]Department of Clinical Pharmacology and Toxicology, Anam Hospital, Korea University College of Medicine, Seoul 02841, Republic of Korea
[6]Department of Neurology, Korea University Anam Hospital, Korea University Medicine, Seoul 02841, Republic of Korea
[7]Division of Clinical Pharmacology, Department of Medicine, Vanderbilt University Medical Center, Nashville, TN 37232, USA
[8]Department of Biomedical Sciences, Graduate School of Medicine, Korea University, Seoul 02841, Republic of Korea

[†]These authors contributed equally

[*]Corresponding author. Email: jyseong@korea.ac.kr

Abstract:

Alzheimer's disease (AD) is characterized by the progressive loss of synapses, leading to cognitive decline. Immunotherapies targeting amyloidosis or tauopathy have shown promise in AD treatment, but additional therapies are needed to inhibit continuous and excessive synaptic loss, which could improve clinical outcomes by modifying the course of the disease. Understanding the mechanisms of synaptic loss is essential for the development of new therapies. Here, we propose an antibody-based immunotherapy targeting FAM19A5, a secretory protein in the brain. We found that FAM19A5 binds to LRRC4B, a post-synaptic adhesion molecule, which disassembles synaptic connections, leading to synapse elimination. FAM19A5 levels increased in association with aging and the progression of tau accumulation. We inhibited FAM19A5 using NS101, an anti-FAM19A5 monoclonal antibody, in mouse models of AD. NS101 preserved synaptic connections despite the presence of amyloid or tau aggregates. Consequently, the number of mature synapses and their function were restored, resulting in improved cognitive performance. In study participants, NS101 was delivered to the human brain across the blood-brain barrier, bound to FAM19A5, and cleared into the peripheral circulation without any toxicity. These findings demonstrate that restoring synapses by inhibiting synaptic elimination can be an effective therapeutic strategy and provide a fundamental basis for modifying AD.

One-Sentence Summary: The antibody NS101 targeting FAM19A5 restores synapse number and function in Alzheimer's disease, improving cognition.

Main Text:

INTRODUCTION

FAM19A5, also known as TAFA5, is a secretory protein primarily detected in neurons of the central and peripheral nervous systems (*1*). Its amino acid sequence remains highly conserved across vertebrate evolution, but conservation between FAM19A families is relatively low, indicating that FAM19A5 has a distinct and crucial function in the brain (*2*, *3*). Recent knockout and genome-wide association studies have revealed that FAM19A5 plays a particularly important role in synapse-related brain function, such as learning and memory, as well as in diseases including Alzheimer's disease (AD), attention deficit hyperactivity disorder, and autism (*4*–*6*). While neurexin serves as a major presynaptic receptor for other FAM19As and participates in a wide range of neurological processes (*7*), it is suggested that FAM19A5 may act as a ligand for different synaptic receptors. This action could be involved in synapse modification, thereby impacting neural function (*8*). However, the mechanisms of the unknown receptor interaction and its effects on synapse regulation in key brain regions, such as the cortex and hippocampus, are yet to be fully understood.

AD is a neurodegenerative disorder characterized by progressive dementia. While there are several therapeutic agents approved to treat AD, they offer only limited symptomatic relief and do not slow the progression of the disease (*9*). Recently, antibody-based immunotherapy against amyloid beta (Aβ) has attracted significant attention following its approval by the US FDA (*10*, *11*). However, synaptic loss that remains and continues after Aβ clearance may limit the efficacy of immunotherapy for cognitive improvement (*12*, *13*). A novel approach targeting synapse loss could be a breakthrough, as it is one of the fundamental hallmarks of AD, causing the loss of connections between neurons and contributing to cognitive deficits (*14*). Understanding the mechanisms behind synapse loss in AD may facilitate the development of more potent treatments (*15*, *16*).

Here, we propose an antibody-based immunotherapy targeting FAM19A5, which can improve cognitive function by restoring synapses in AD. We identified LRRC4B, a post-synaptic adhesion molecule, as a receptor for FAM19A5. FAM19A5 contributes to the dissociation of the interaction between LRRC4B and PTPRF, a presynaptic adhesion molecule, which may eventually lead to synapse elimination. FAM19A5 in human cerebrospinal fluid was found to increase in proportion to aging and tau accumulation, suggesting that FAM19A5 is an accelerator of synaptic elimination. We found that inhibiting FAM19A5 with a competitive protein derived from LRRC4B can suppress this elimination. Inspired by these mechanisms of synaptic elimination, we developed NS101, a potent monoclonal antibody against FAM19A5, to prevent excessive synapse loss in AD. Systemic injection of NS101 in AD mice suppressed synapse elimination to wild-type levels, restoring mature synapse number and cognitive behaviors to normal. Our findings suggest that targeting FAM19A5-LRRC4B complex formation could offer a promising therapeutic approach for AD.

RESULTS

FAM19A5 binds to the FB domain of LRRC4B.

We hypothesized that FAM19A5 might interact with other synaptic adhesion molecules to induce either synapse formation or elimination (Fig. 1A), as other members of the FAM19A family bind to neurexin, but FAM19A5 does not interact with it in the same manner (*8*). To explore potential binding molecules for FAM19A5, we investigated RNA expression patterns

from 168 types of neurons in the mouse brain scRNA-seq database (*17*), comparing their correlation with *fam19a5* to narrow down candidates. We found that the expression of *lrrc4b*, a post-synapse adhesion molecule, was highly correlated with *fam19a5*, suggesting a possible interaction in the synaptic cleft (Fig. 1B and fig. S1). Given their similar expression patterns and their secretion into the cerebrospinal fluid (CSF) (*18–20*), we expected that FAM19A5 and LRRC4B would exist in a complex form in the CSF. To determine the potential interaction, we conducted co-immunoprecipitation (co-IP) with human CSF. We selectively captured FAM19A5 from human CSF using its monoclonal antibodies against each N- and C-terminal region of FAM19A5 and separated them by size through western blotting to identify bound proteins. Indeed, LRRC4B was co-immunoprecipitated with the antibody that binds to the C-terminal region of FAM19A5, indicating that FAM19A5 and LRRC4B interact and are secreted into human CSF in a complex form (Fig. 1C).

To evaluate the cellular relevance of this interaction, we co-expressed FAM19A5 and LRRC4B in HEK293 to analyze their protein expression patterns. Both proteins were predominantly colocalized along the plasma membrane, suggesting that FAM19A5 interacts with LRRC4B (Fig. 1D). The interaction of these proteins was further confirmed by additional immunoblotting assays with the co-expressing cell and medium. We observed that the concentration of secreted FAM19A5 in the medium significantly decreased, while its concentration markedly increased in lysates upon co-expressing LRRC4B (Fig. 1E). These results demonstrate that LRRC4B is a specific adhesion molecule for FAM19A5.

To determine which domain of LRRC4B interacts with FAM19A5, we generated various LRRC4B fragments with different domains and performed co-IP assays. We found that LRRC4B fragments containing the amino acids at positions 484-498 interacted with FAM19A5 (fig. S2A). Using ELISA, we then tested this interaction under purified conditions, confirming both binding affinity and interaction. In line with the co-IP results, FAM19A5 exhibited high affinity for LRRC4B fragments within the amino acid range 484-498 (EC_{50} values were 68.5 pM for the sequence 453-576 and 112.1 pM for 484-576). In contrast, no binding was evident without the sequence (Fig. 1F). These results demonstrate that the sequence 484-498 of LRRC4B acts as a FAM19A5 binding domain, termed the FB domain.

To elucidate the essential residues within the FB domain, we evaluated the binding free energy and compared its changes after Ala substitution of each residue. Predictions indicated that all residues, except Thr494 and Leu495, played vital roles in binding (fig. S2B), which was further supported by ELISA results (fig. S2C). We also determined the key residues of FAM19A5 for LRRC4B binding. Residues Arg58, Arg59, Arg125, and Lys127 of FAM19A5 were predicted as significant binding residues (fig. S2D). Subsequent ELISAs demonstrated that Arg125 and Lys127 were significant, while Arg58 and Arg59 were moderate for LRRC4B binding (Fig. 1G). A surface plasmon resonance (SPR) measurement showed the equilibrium dissociation constant (K_D) of the FAM19A5-LRRC4B complex at 32 pM (fig. S2E), demonstrating their pronounced binding affinity, which stands out when juxtaposed with bindings of other synaptic adhesion molecules (*21*). Interestingly, the amino acid sequence of the FB domain is highly conserved across vertebrate species, including humans (fig. S2F). This conservation implies that its interaction with FAM19A5 and the function of the FAM19A5-LRRC4B complex could be crucial and evolutionarily preserved in vertebrates.

Next, we undertook 3D modeling of the FAM19A5-LRRC4B complex to delve into their structural and molecular interactions. After constructing models of the complex (*22–24*), we observed that they interacted through the key residues of FAM19A5 and the FB domain of

LRRC4B, as illustrated in Fig. 1, F and G. The sequence of FB, which exhibited a disordered structure prior to binding with FAM19A5, transformed into a β-strand. The β-strand then interacted with the β-strands of FAM19A5, primarily via hydrogen bonds (Fig. 1, H and I). Furthermore, predictions indicated the formation of a salt bridge between LRRC4B Glu493 and FAM19A5 Lys127, one of the pivotal residues for binding. This interaction likely further stabilized the complex structure (Fig. 1J).

FAM19A5 binding to LRRC4B leads to the dissociation of synaptic contacts.

Given that LRRC4B forms a trans-synaptic connection with PTPRF, a pre-synaptic molecule primarily found in excitatory neurons, within the synaptic cleft (*25*), we postulated that FAM19A5 binding to LRRC4B might induce a conformational change in the LRRC4B-PTPRF connection, resulting in synapse modification. To test this hypothesis, we performed ELISAs to quantitatively evaluate the LRRC4B-PTPRF binding and detected changes in binding in the presence of either wild-type (WT) or mutant (MT) FAM19A5. We found that WT FAM19A5 significantly inhibited LRRC4B-PTPRF binding in a dose-dependent manner, whereas MT FAM19A5 only partially dissociated the binding (Fig. 2A, IC_{50} of WT FAM19A5: 281 nM). This result suggests that the dissociation of the LRRC4B-PTPRF complex by FAM19A5 could lead to synapse loss.

To investigate this further, we treated FAM19A5 in primary hippocampal neurons expressing FAM19A5, LRRC4B, and PTPRF from an early stage (fig. S3). We observed that the addition of WT FAM19A5 significantly decreased the expression of both the pre- and post-synaptic markers, synaptophysin (SYP) and postsynaptic density protein 95 (PSD95), compared to the control (Fig. 2, B and C). On the other hand, the MT FAM19A5 led to a milder decrease in expression compared to the control. These decreases were also evident in the colocalization of the synaptic markers, indicating that FAM19A5 binding to LRRC4B causes the dissociation of LRRC4B-PTPRF, resulting in synapse loss.

Having established that FAM19A5 dissociates the LRRC4B-PTPRF complex and leads to synapse loss, we hypothesized that blocking FAM19A5 with the synthetic FB-containing protein could inhibit FAM19A5 binding to LRRC4B, thereby preserving synaptic connections (Fig. 2D). To validate this, we measured FAM19A5-LRRC4B binding in the presence of WT or MT FB protein. We observed that the WT FB protein effectively inhibited the binding of FAM19A5 to LRRC4B in a dose-dependent manner, whereas the MT FB protein had minimal impact (Fig. 2E). This implies that blocking the interaction between FAM19A5 and LRRC4B could prevent synapse loss and increase synapse density. To corroborate this, we exposed primary hippocampal neurons to FB proteins and evaluated the expression of synaptic markers. The intensity and colocalization of these markers were significantly increased by WT FB protein but not by MT FB protein compared to the control (Fig. 2, F and G). This confirms that inhibition of FAM19A5 binding to LRRC4B boosts synapse density by preventing synapse loss.

NS101, a potent monoclonal antibody against FAM19A5.

In an effort to understand the mechanisms underlying synapse loss and to develop therapeutic strategies for neurodegenerative diseases such as AD, we generated NS101, a monoclonal antibody targeting FAM19A5. NS101 displayed specificity, binding exclusively to FAM19A5 among the FAM19A family members (Fig. 3A). ELISAs using FAM19A5 fragments demonstrated that the epitopes for NS101 were Arg52, Pro57, Arg58 and Arg59 (fig. S4A). Notably, Arg58 and Arg59 are key residues of FAM19A5 for its binding to LRRC4B, indicating that NS101 can inhibit FAM19A5-LRRC4B complex formation by competitively

binding to these key residues. SPR measurements showed that NS101 has a strong affinity for FAM19A5 (fig. S4B. K_D =111 pM). Owing to this high affinity, NS101 effectively dissociated the FAM19A5-LRRC4B complex more than the synthetic FB protein (Fig. 3B, IC_{50} for NS101: 0.2 nM vs. IC_{50} for FB protein: 8 nM).

To evaluate the pharmacokinetics of NS101, we monitored its concentration in rat blood following a single intravenous (IV) administration. NS101 was gradually excreted from the body over a span of 28 days, with a half-life of 7.5 days for a dose of 10 mg/kg and 11.7 days for a dose of 50 mg/kg (Fig. 3C). Systemic exposure to NS101 was increased in a dose-dependent manner, as evidenced by the area under the curve (AUC, 10,336.3 hour·µg/mL for a dose of 10 mg/kg and 54,415.0 hour·µg/mL for a dose of 50 mg/kg). Similar to clinical antibodies (*26*), prolonged systemic exposure to NS101 facilitated its delivery to the brain across the blood-brain barrier (BBB). In the mouse brain, NS101 reached its peak concentration 30 hours after a 10 mg/kg IV injection. Subsequently, NS101 levels declined slowly over 28 days with a half-life of 17.3 days (Fig. 3D). Based on the 28-day AUC, the plasma-brain antibody ratio indicated that approximately 3% of plasma NS101 reached the brain, which was comparable to the clinical antibody for Aβ (*11*). NS101 in the brain was either excreted directly to the blood vessels or transported via the CSF. NS101 reached its highest concentration in the rat CSF 36 hours after a single IV injection (Fig. 3E), and 0.06% of plasma NS101 was transported to the CSF, as per the 28-day plasma-CSF antibody ratio.

To assess the target engagement of NS101, we tracked the concentration of FAM19A5 in plasma originating from the brain over 28 days. Typically, the concentration of FAM19A5 in plasma is negligible (fig. S4C). However, after a single administration of NS101, the concentration of FAM19A5 in plasma surged, peaking at 24 hours, and then declined steadily over the subsequent 28 days (Fig. 3F). This pattern suggests that FAM19A5 was released from the brain upon interaction with NS101, resulting in a plasma FAM19A5 profile that mirrors the concentration profile of NS101 in both the brain and CSF. Additionally, infusing the brain with recombinant FAM19A5 amplified the levels of plasma FAM19A5 when NS101 was administered. In contrast, an infusion of MT FAM19A5 did not produce a similar effect (Fig. 3G). This implies that FAM19A5, when bound to NS101, was cleared from the brain, leading to elevated FAM19A5 levels in the plasma and a consequent reduction in the brain's FAM19A5 levels. Notably, even after repeated administration of high doses, NS101 did not show any long-term toxicity (fig. S4, D and E).

The high interspecies conservation of FAM19A5 sequences led us to hypothesize that the role of FAM19A5 in synapse loss is also identical in humans. To confirm that NS101 delivered to the brain in humans binds to FAM19A5 and is secreted into the CSF followed by the blood, we conducted a clinical trial on a total of 64 healthy subjects. The subjects were divided into 8 groups, with 2 subjects in each group receiving a placebo. The antibody dose was set at 0.25-48.0 mg/kg. The concentration of IV infused NS101 in the serum increased rapidly, with a median T_{max} of 0.98 to 1.74 hours across the doses. Subsequently, NS101 levels slowly decreased over 60 days (Fig. 3H). Antibodies delivered to the brain across the BBB were secreted into the CSF. NS101 secreted into the CSF was detected from the 6 mg/kg dose group and above, and the detected amount showed a tendency to increase in proportion to the dose (Fig. 3I). In the placebo group, only approximately 0.3 ng/ml of plasma FAM19A5 was detected, which was not noticeably changed over time. In contrast, the peak concentration and time of plasma FAM19A5 significantly increased in a dose-dependent manner following the administration of NS101, as determined by the time to maximum effect (median TE_{max} of 11.96 to 95.55 hours). NS101 at more than 6 mg/kg did not distinctly increase the peak concentration of FAM19A5 but increased the total amount of plasma FAM19A5 in a manner proportional to

the dose (AUC range from 707843.52 to 7730521.14 hour·pg/mL) (Fig. 3J). In addition, no dose-related adverse events, including serious side effects and death, were found in any of the experimental groups. These results demonstrate that NS101 can target FAM19A5 in humans in the same way, which strongly suggests the possibility of synapse restoration due to decreased FAM19A5 in the AD brain.

NS101 prevents synapse loss, increasing functional synapses in mouse models of AD.

To determine whether NS101 inhibition of FAM19A5 leads to an increase in synapse numbers, we examined the expression of two synaptic markers, SYP and PSD95, in cultured neurons treated with NS101. Both the expression of these markers and their colocalization were significantly increased by NS101 (Fig. 4A). To ascertain whether these increases correlated with a rise in synapse numbers, we assessed the spine density in dendrites. We found a significant increase in dendritic spines after NS101 treatment (Fig. 4B).

Progressive loss of synapses is a common pathological condition in aging (*27*) and AD (*14*, *28*), suggesting that FAM19A5 may contribute to synaptopathy-related disorders. Indeed, we observed that the concentration of FAM19A5 in human CSF increased with age (fig. S5A). In addition, the concentration of CSF tau proteins, including phospho-tau (p-tau), which is the primary component of neuronal tangles in AD (*29*), rose in parallel with FAM19A5 levels (fig. S5B). Given the observed correlation between CSF FAM19A5 and tau proteins, we hypothesized that NS101 inhibits the increased FAM19A5 in AD, which could restore synapse numbers. To investigate this, 6-month-old P301S mice, known to exhibit progressive synapse loss in the cortex due to accumulating p-tau proteins (*30–32*), were IV administered 10 mg/kg NS101 weekly for 4 weeks. P301S mice at 7 months old showed a notable reduction in spine density in the prefrontal cortex when compared to their WT littermates. In particular, there was a marked reduction in mushroom spines, mature spines capable of signal transmission (Fig. 4C). However, after NS101 administration, the mushroom spine density rebounded, reaching levels seen in WT mice (Fig. 4D). Meanwhile, the densities of other spine types remained relatively unaffected by NS101 treatment.

The increase in mushroom spine number induced by NS101 might arise from either an enhancement of synapse formation or prevention of ongoing synapse loss. To discern the cause, we employed two-photon live imaging to observe spine changes in the somatosensory cortex of P301S mice following NS101 treatment (Fig. 4E). Compared to WT mice, P301S mice exhibited a significantly higher rate of spine elimination. Interestingly, there was no significant difference in the spine formation rate between the groups. However, after administering two systemic injections of NS101 at weekly intervals, the spine elimination rate notably decreased approximately 1 week after each treatment. This reduction was consistent across both injections and approached the elimination rates observed in WT mice (Fig. 4F). The suppressive effect on spine elimination persisted for up to 2 months, albeit not reaching statistical significance (fig. S5C). These findings demonstrate that NS101 inhibition of FAM19A5 in AD serves to counteract the ongoing loss of synapses.

NS101 restores synaptic activity and cognitive behavior in mouse models of AD.

Given that NS101 increased the density of mature spines, we determined whether this increase was associated with enhanced synaptic functions in AD. APP/PS1 mice, which exhibit synapse loss associated with amyloid beta plaques, were used to assess the synaptic function after NS101. 13-month-old APP/PS1 mice received IV administration of NS101 weekly for 4 weeks. Subsequently, we measured the miniature excitatory postsynaptic currents (mEPSCs)

in the CA1 pyramidal neurons of the hippocampus. The frequency of mEPSCs, which arise from the spontaneous release of neurotransmitters, was significantly reduced in APP/PS1 mice compared to their WT littermates. NS101 treatment, however, restored the mEPSC frequency to levels comparable to those of WT littermates (Fig. 5A), aligning with observations of enhanced synapse marker proteins in the hippocampus by NS101 (fig. S6). These findings, along with the slightly increased mEPSC amplitude (Fig. 5B), suggest that NS101 strengthened synaptic function. The synaptic strengthening by NS101 was further confirmed through field excitatory postsynaptic potential (fEPSP) measurement, revealing enhanced fEPSP slopes and fiber volley amplitudes (Fig. 5C). Consequently, this facilitated the induction and maintenance of long-term potentiation (LTP) at normal levels in APP/PS1 mice (Fig. 5D).

Next, we investigated whether synaptic potentiation results in cognitive improvement. In the Y maze test, the spontaneous alternation rate of NS101-treated APP/PS1 mice improved to the level of WT mice, while there was no significant difference in the total arm entry number across all groups (Fig. 5E). This suggests that NS101 improved the short-term memory of the APP/PS1 mice. In the passive avoidance test, all groups showed no difference in the initial memory acquisition to avoid electric shocks. Although APP/PS1 mice exhibited a significant decline in memory 24 hours after learning, NS101-treated mice maintained memory levels comparable to those of WT mice (Fig. 5F). This indicates that NS101 enhanced the long-term memory of the APP/PS1 mice. We then conducted the Morris water maze test with P301S mice (Fig. 5G). All groups exhibited similar locomotion abilities, as evidenced by the total distance traveled (Fig. 5H). P301S mice took significantly longer to locate the platform than WT mice. However, NS101-treated P301S mice found the platform in a significantly shorter time (Fig. 5I). NS101-treated P301S mice performed at a similar level to WT mice in terms of quantitative indicators such as platform crossing and spatial preference (Fig. 5, J and K). These results suggest that NS101 ameliorated the spatial learning and memory deficits associated with AD.

DISCUSSION

Synaptic loss is a common pathological feature in age-related neurodegenerative diseases, including AD, and is a central convergence point for the diverse causes and environments that promote these diseases (*14*, *28, 29*). Synapses naturally form and are lost throughout one's life, serving as a crucial mechanism for modulating neural plasticity (*33*, *34*). However, in the context of neurodegenerative diseases, the rate of synaptic loss outpaces that of synapse formation. This imbalance results in a net decrease in synapses, which subsequently leads to compromised cognitive function, motor control, and other neurological manifestations. Importantly, synaptic loss often emerges early in disease progression (*35*), suggesting potential reversibility in some instances. This may present a window of opportunity for intervention to prevent or reverse the disease process. Deepening our understanding of the mechanisms governing synapse dynamics could pave the way for more potent treatments for neurological diseases.

This study highlights the FAM19A5 protein as a significant contributor to synapse loss. FAM19A5 interacts with the FB domain of LRRC4B, leading to synapse reduction in neurons. Conversely, either the synthetic FB protein or the monoclonal antibody NS101, which acts by competitively inhibiting FAM19A5's function, augments the synapse count in neurons.

AD is characterized by significant synapse loss, largely attributed to the accumulation of Aβ and p-tau proteins and their cytotoxicity in the aging brain (*14*). We investigated whether

treatment with NS101 could restore lost synapses in the presence of aggregates. Compared to WT mice, tauopathy P301S mice exhibited fewer spines, resulting from an elevated rate of spine loss rather than a reduced rate of spine formation. However, when P301S mice were treated with NS101, their rate of synapse loss diminished to levels observed in WT mice, restoring their synapse numbers to standard levels. Moreover, NS101 normalized synapse numbers but also enhanced synapse functionality and cognitive performance in APP/PS1 mice exhibiting amyloidosis. These findings underscore the role of FAM19A5 in influencing the rate of synapse loss in AD pathology. Recent single-cell/nuclear RNA-seq analyses from human samples revealed heightened FAM19A5 transcript levels in AD brain neurons (*36*) and especially in tau-tangle-bearing neurons (*37*), indicating a potential link between FAM19A5 and AD.

The recent proposition that restoring synaptic connections could be a groundbreaking strategy for AD treatment, was supported by a study in which a synthetic synapse organizer, when directly infused into the hippocampus, rejuvenated synaptic function and enhanced cognitive behavior (*21*). However, the clinical application of this synapse organizer is limited due to its invasiveness for delivery and long-term instability. To address these challenges, we introduced the monoclonal antibody NS101 as a non-invasive and stable alternative, paving the way for human clinical trials. Indeed, systemically administered NS101 can cross the BBB and facilitate the stable transport of FAM19A5 to peripheral circulation for approximately 59 days in humans. The identical amino acid sequences of FAM19A5 and the FB domain of LRRC4B across mice, rats, and humans further enhance NS101's potential in human trials. Given that NS101 binds equally well to both mouse and human FAM19A5, the effects of NS101 on the FAM19A5-LRRC4B complex observed in animal experiments hold promise for replication in human clinical studies.

While synapse loss is a pivotal early pathological event in AD, yet most clinical studies have focused on clearing hallmark pathologies such as accumulated Aβ and p-tau. Despite their efficacy in removing these proteins, many antibody drugs targeting Aβ and p-tau have not shown significant improvement in cognitive decline in AD patients (*38*, *39*). Only a few drugs have been recently approved for further evaluation of their ability to improve cognitive function in these patients (*40*, *41*). Hence, finding a target protein that can normalize synapse dynamics in the AD brain could open up new avenues for therapeutic intervention that complement strategies for eliminating Aβ and p-tau. In this context, FAM19A5, as a suppressor of synapse formation, could be a promising target for AD. Therapies counteracting FAM19A5, such as the NS101 approach, may offer promising strategies for treating neurodegenerative diseases, including AD.

MATERIALS AND METHODS

Human samples

Pooled normal human cerebrospinal fluid (CSF) was obtained from Innovative Research, Inc. (IPLA-CSFP) and used for the co-IP experiment to determine the association between FAM19A5 and LRRC4B. Individual human CSF and plasma samples were obtained from BIOIVT & ELEVATING SCIENCE and were used to measure age-dependent FAM19A5 levels in CSF and the basal level of FAM19A5 in plasma, respectively. Additionally, individual human CSF samples were also used to determine total tau and phospho-tau levels.

Vertebrate animals

C57BL/6J mice (strain No. 000664), APP/PS1 [B6. Cg-Tg (APPswe, PSEN1dE9) 85Dbo/J] mice (Strain No. 034832-JAX), and P301S [B6. C3-Tg (Prnp-MAPT*P301S) PS19Vle/J] mice (strain No. 008169) were purchased from The Jackson Laboratory. Sprague–Dawley rats and cynomolgus monkeys were obtained from Orient Bio. The mice were housed under temperature-controlled conditions (22–23°C) with a 12-h light/12-h dark-light cycle (lights on at 8:00 am) and had ad libitum access to standard chow and water. The behavioral tests were conducted by NDIC, in accordance with the Animal Protection Act (Law No. 4372 enacted on May 31, 1991, partially revised Act No. 13023 on January 20, 2016) and approved by the Animal Experimentation Ethics Committee of KPC Co., Ltd. (Approval No. P191005). The procedures related to the analysis of animal samples were further approved by the Institutional Animal Care and Use Committee of Korea University (KOREA-2020-0031, KOREA-2020-0037, and KOREA-2021-0002). Ethical regulations were followed throughout.

Cell lines

HEK293 cells (ATCC# CRL-1573) were cultured in a humidified incubator at 37°C with 5% CO_2. HEK293 cells were propagated in MEM with GlutaMAXTM (Gibco) supplemented with 10% fetal bovine serum (Gibco) and 100 U/ml penicillin–streptomycin (Gibco). For subculture, cells were washed with DPBS (Gibco) and dissociated in 0.25% trypsin-EDTA (Gibco) for 5 min at 37°C.

DNA constructs

The pCMV20-Igκ_SP-FLAG vectors used for cloning were constructed by inserting a human Igκ signal peptide (SP) sequence in front of the FLAG tag of the pCMV20 plasmid (Sigma). Full-length (36-713) and serial deletion constructs (36-363, 36-576, 157-713, 230-713, 364-713, 453-713, 577-713, 364-576, *364-576, 453-576, 484-576 and 498-576) of human LRRC4B (NM_001080457.1) were constructed in the pCMV20-Igκ SP-FLAG vector. The pCMV20-Igκ SP-hFc vector inserted Igκ SP at the N-terminus of MCS (multiple cloning site) and human-Fc (hFc) at the C-terminus in the pCMV20 plasmid. The ectodomain (36-576) and fragment (453-576) of human LRRC4B were constructed into the MCS of the pCMV20-Igκ_SP-hFc vector. Mutant constructs in which Thr488 and Thr489 of LRRC4B were substituted with Ala or Ser were subcloned and inserted into the pCMV20-Igκ_SP-FLAG or pCMV20-Igκ_SP-hFc vector. FAM19A5 (WT and MT) and LRRC4B fragments (36-576 and 453-576) were inserted into the pCAG1.1-Igκ_SP-His-TEV vector. Mutant constructs in which Arg58, Arg59, and/or Arg125, Lys127 of FAM19A5 are substituted with Ala were subcloned and inserted into the pCAG1.1-Igκ_SP-His-TEV vector. Full-length human LRRC4B was subcloned and inserted into the pcDNA6-V5-His vector (Invitrogen). FAM19A5 (NM_001252310.1) without tags was subcloned and inserted into the pcDNA3.1 vector (GenScript). The ectodomain (30-1263) of PTPRF (NM_002840.4) was inserted into the pCMV20-Igκ_SP-hFc vector. All cloning was performed using the AccuRapid™ Cloning Kit (Bioneer) according to the manufacturer's instructions. The primer sets used for cloning are listed in table S1. Full-length human LRRC4B (OHu30422) and PTPRF (OHu02063) plasmid DNAs were purchased from GenScript.

Purification of recombinant proteins

Recombinant His-tagged proteins were purified according to the method described previously (*42*). In brief, FAM19A5 (WT and MT) and LRRC4B(36-576) with N-terminal 6xHis tags, followed by a tobacco etch virus protease (TEV) recognition sequence, were cloned and inserted into the pCAG1.1 vector (a gift from Jong-Ik Hwang) and expressed in Expi293F cells (Gibco, A14527). The supernatant containing His-TEV-FAM19A5 was collected for Ni-NTA affinity chromatography (Cytiva). After washing with a binding buffer containing 20 mM Tris-HCl (pH 7.5) and 200 mM NaCl, the proteins were eluted using binding buffers with increasing concentrations of imidazole (from 5 to 500 mM). Proteins eluted from 50 to 500 mM imidazole fractions were concentrated using Amicon® Ultra15 Centrifugal Filter Units (Millipore), and the buffer was exchanged for 1x DPBS (Gibco). The purified His-TEV-FAM19A5 proteins were digested overnight at 30°C with AcTEV protease (Invitrogen) to remove the His-tag and TEV sequence. The AcTEV protease containing the His-tag was then eliminated by overnight incubation with Ni-NTA, and digestion was confirmed using an anti-His tag antibody (Abcam). LRRC4B (ectodomain and fragments) and PTPRF (ectodomain) were cloned and inserted into the pCMV20-Igκ_SP-hFc vector and expressed in Expi 293F cells. The supernatant containing hFc-fused proteins was collected using rProtein A GraviTrap (Cytiva), and the hFc-fused proteins were eluted using an Ab buffer kit (Cytiva) following the manufacturer's instructions.

Production of anti-FAM19A5 antibodies

We generated two chimeric chicken/human monoclonal antibodies against FAM19A5, named N-A5-Ab and C-A5-Ab, by immunizing chickens (Gallus gallus domesticus) with purified recombinant FAM19A5 using a previously described method (*42*). The N-A5-Ab and C-A5-Ab were further deimmunized and optimized by amino acid substitution to generate NS101 and SS01, respectively.

Production of protein fragments

To elucidate the key residues in the FB domain of LRRC4B for FAM19A5 binding, we custom-made mutant peptides in which each single residue was substituted with Ala or Asn. The amino acid sequences are listed in table S2. To identify the epitopes of the FAM19A5 antibodies, the FAM19A5 linear sequence was divided into six groups, labeled F1 to F6. Further analysis was conducted to determine the crucial residue for binding, in which each single residue in F2 was replaced with Ala. The relevant proteins and their amino acid sequences are listed in table S3 and S4.

Electroporation and co-IP

HEK293 cells were transfected with the NeonTM transfection kit (Invitrogen) according to the manufacturer’s description. For the general co-IP experiments, after transfection, cells were treated with FAM19A5 for 30 min. The cells were washed twice with cold phosphate-buffered saline (PBS) and resuspended in lysis buffer containing 20 mM Tris-HCl (pH 7.4), 150 nM NaCl, 0.5% NP40, and a protease and phosphatase inhibitor cocktail (Thermo). The supernatants were isolated by centrifugation at 12,000 × g at 4°C for 30 min and then mixed with 30 µl of Protein G Dynabeads (Invitrogen) that had been preincubated with antibodies. The mixtures were incubated at 4°C overnight in a rotating mixer. The beads were spun down and washed three times with 20 mM Tris-HCl (pH 7.4), 300 mM NaCl, and 0.5% NP40 in washing buffer. After adding 30 µl of 2× sample buffer containing a reducing agent to the beads

and boiling at 100°C for 10 min, the proteins were separated by SDS–PAGE. For human CSF co-IP, pooled human CSFs (Innovative Research) were mixed with 0.5% NP40 and 50 µl of Pierce Protein A/G Plus Agarose (Thermo) that had been preincubated with 10 µg anti-human IgG, N-A5-Ab, and C-A5-Ab. The mixtures were rotated at 4°C overnight and washed three times. The protein complex in the beads was resolved by SDS–PAGE.

Immunoblots

Cells were homogenized and prepared in lysis buffer containing 20 mM Tris-HCl (pH 7.5), 500 mM NaCl, 5 mM $MgCl_2$, and protease inhibitor cocktail (Thermo). The primary antibodies are described in table S5. Immunoblots of cells were performed as described previously (*42*).

Phase 1 trial of NS101

The study NCT05143463 is a phase 1, double-blind, randomized, placebo-controlled, first-in-human (FIH) clinical trial designed to evaluate the safety and tolerability, as well as pharmacokinetic (PK), pharmacodynamic (PD), and immunogenicity profiles of study NS101 in healthy subjects under fasting conditions. We selected a healthy male volunteer population for this study because healthy subjects without any concomitant diseases or medications are a homogenous population, which allows for proper evaluation of NS101's safety, tolerability, and PK without confounding factors. We assessed subjects against the inclusion and exclusion criteria, which were described in our clinical report (NCT05143463), to determine if they were eligible to participate in this study. All subjects were provided with informed consent forms (ICFs) in their preferred language (either French or English) for review. Prior to initiation of study procedures, the ICF was verbally reviewed with the subjects by qualified staff, allowing sufficient time for review of the information provided and to answer any questions subjects had. Subjects were informed of any developments or changes to procedures that could influence their continued participation in the study. Subjects did not anticipate any direct benefits from participation in this research study, with the exception that they received a health evaluation. Subjects who participated in this study were compensated for their time; however, they were not offered any incentives.

NS101 infusion doses of 0.25, 0.75, 1.5, 3.0, 6.0, 12.0, 24.0, and 48.0 mg/kg (cohorts 1 to 8) were selected based on nonclinical pharmacology, PK, and toxicology studies in rats and monkeys. The study consisted of 8 cohorts, each including 8 subjects, randomized in a 3:1 ratio (6 subjects received NS101 and 2 receiving matching placebo), for a total of 64 subjects. For every cohort, the body weight of each subject measured the day before was used to calculate the exact individual dose required on a mg/kg basis based on their assigned dose level. The drug was administered on the morning of the day after subjects had fasted overnight for at least 8 hours. The cohorts were dosed sequentially in an ascending fashion. The IV infusion was performed over a period of approximately 60 minutes in bed using aseptic techniques at a constant rate using a volume-controlled infusion device. At the end of the infusion, 3 mL of saline solution was injected to flush the remaining drug into the IV catheter. The end of infusion was set to the end of the 3 ml flush.

In each cohort, a total of 21 blood samples were drawn into blood collection tubes (1 x 3 mL) containing plastic serum spray-coated silica at prestart of infusion and 0.25 (±3 min), 0.5 (±3 min), 0.75 (±3 min), 1 (±3 min), 1.25 (±3 min), 1.5 (±3 min), 2 (±3 min), 4 (±3 min), 6 (±3 min), 8 (±3 min), 12 (±15 min), 24 (±15 min) (Day 2), 36 (±15 min) (Day 2), 48 (±15 min)

(Day 3), 96 (Day 5±1), 168 (Day 8±1), 336 (Day 15±1), 504 (Day 22±2), 672 (Day 29±2), and 1416 (Day 60±3) hours post-start of infusion. Blood samples were kept at room temperature and were centrifuged at 1300 ±20 g for at least 10 minutes at room temperature (no more than 180 minutes passed between the time of each blood draw and the start of centrifugation). Two aliquots of at least 0.5 mL (when possible) of serum were dispensed into polypropylene tubes as soon as possible. The aliquots were stored at -80°C until ELISA.

Subjects assigned to Cohorts 5 through 8 were randomized for collection of a CSF sample at one of the following timepoints: 24 (±3 horus), 36 (±3 horus), 168 (day 8±1), or 336 (day 15±1) hours post-start of infusion. Each of the 4 timepoints was assigned to 2 subjects. Sentinel subjects were randomized to the same timepoint to ensure that each timepoint was assigned to at least 1 subject receiving NS101. A single CSF sample was collected via lumbar puncture. The volume of collected CSF per sample did not exceed approximately 6 ml. A stabilizing agent (10% BSA in 1X PBS with 5% Tween-20) was added and mixed with the NS101 CSF samples (no more than 8 minutes between sample collection and mixing with the stabilizing agent). Two aliquots of at least 0.5 mL (when possible) of CSF were dispensed into polypropylene cryovials as soon as possible. The aliquots were stored at -80°C (±10°C) until ELISA.

The clinical study protocol, any relevant associated documents, and ICFs were reviewed and approved by an Institutional Review Board (IRB, #00000971) prior to beginning the associated study procedures. The ethics committee that reviewed the study was Advarra, an independent service provider located in Aurora, Ontario, Canada. The IRB had no representatives from Syneos Health or Sponsor and was, therefore, completely independent. All clinical work was conducted in compliance with Good Clinical Practices (GCP) as referenced in the International Council for Harmonization (ICH) guidelines (ICH E6), Good Laboratory Practices (GLP) as referenced in the ICH guidelines, and all applicable regulations, including the Federal Food, Drug and Cosmetic Act, U.S. applicable Code of Federal Regulations (CFR) Title 21, and any IEC requirements relative to clinical studies.

ELISA

To evaluate both total and phosphorylated tau levels, ELISA kits, such as hTAU Ag (Fujirebio) and PHOSPHO-TAU (Fujirebio), were used according to the manufacturer's instructions.

For the measurement of FAM19A5 in biofluids, we coated 96-well microplates with LRRC4B (453-576) protein, which was diluted in a 50 mM carbonate buffer (pH 9.6) to achieve a final concentration of 1 µg/ml. These plates were sealed and incubated overnight at 4°C. The following day, we washed the plates twice with 300 µL of washing buffer (PBS with 0.05% Tween 20) per well using a microplate washer (Tecan, Hydroflex) and gently tapped them on a paper towel to remove any remaining solution. Subsequently, 200 µl of blocking buffer was added to each well, and the plates were sealed and incubated at 37°C for 1 hour. After two additional washes, 100 µl of both the standard solution and samples were added to each well. The plates were sealed and incubated at room temperature for 90 minutes. Following another five washes, 100 µl of HRP-conjugated C-A5-Ab, diluted in blocking buffer (PBS with 1% BSA and 0.05% Tween 20) to a final concentration of 0.2 µg/ml, was added to each well and incubated at 37°C for 1 hour. Then, 100 µl of TMB solution (Thermo Fisher, 34029) was added to each well and incubated at room temperature for 20 minutes. To stop the colorimetric reaction, 100 µl of 1 N sulfuric acid was used, and the optical density (OD) value of each well was determined using a microplate reader (Molecular device, VERSA max) at 450 nm.

Depending on the specific experimental objectives, we made adjustments to the proteins and antibodies used for capture and detection while keeping all other procedures consistent. To measure CSF NS101, we employed a pair of rabbit anti-human IgG heavy chain antibodies (Invitrogen) and HRP-conjugated goat α-human IgG kappa light chain antibodies (Thermo).

To assess the binding affinity between FAM19A5 and the LRRC4 family, we utilized various LRRC4/4B/4C deletion proteins, including LRRC4(39-527), LRRC4B(36-576), LRRC4B(453-576), LRRC4B(484-576), LRRC4B(498-576), and LRRC4C(45-527), as capture agents. We used both WT and MT FAM19A5 proteins, including FAM19A5(R58A, R59A), FAM19A5(R125A, K127A), and FAM19A5(R58A, R59A, R125A, K127A), for binding analysis. Detection was carried out using HRP-conjugated C-A5-Ab.
To examine the inhibition of FAM19A5-LRRC4B binding, we initially coated the plate with LRRC4B(453-576) protein. Subsequently, we added the test sample and FAM19A5 protein. The degree of binding inhibition was determined by detecting FAM19A5 using HPR-conjugated C-A5-Ab. For the PTPRF-LRRC4B binding inhibition test, LRRC4B(36-576) protein was coated on the plate, followed by the addition of the test sample and PTPRF protein. The binding inhibition was calculated by detecting PTPRF-hFc using an anti-human IgG Fc antibody.

Surface plasmon resonance (SPR)

SPR experiments were carried out on a Biacore 8K (Cytiva, for affinity between NS101 and FAM19A5) or a Biacore t200 (Cytiva, for affinity between FAM19A5 and LRRC4B) with active temperature control at 25°C following the manufacturer's protocols. The running buffer was 1 × HBS-EP (10 mM HEPES, 150 mM NaCl, 3 mM EDTA, 0.05% Tween 20, pH 7.4). For immobilization, 6xHis-LRRC4B(453–576) in 10 mM sodium acetate, pH 4.5 buffer equivalent to 0632–638 resonance units (RU), was injected onto a nitrilotriacetic acid (NTA) chip at a 30 µl/min flow rate. Increasing concentrations (0.78, 1.56, 3.12, 6.25, and 12.5 nM) of FAM19A5 were diluted in running buffer and flowed across the immobilized 6xHis-LRRC4B(453–576) for 180 s at a flow rate of 30 µl/min (association). The sample was replaced with a running buffer for 240 s (disassociation). The chip surface was regenerated with 350 mM EDTA and HBS-P 500 mM imidazole. For all samples, blank injection with buffer alone was subtracted from the resulting reaction surface data. Data were analyzed using Biacore 8K evaluation software (Cytiva).

In silico modeling of the FAM19A5-LRRC4B

We used AlphaFold2 (*24*) to model the structure of the FAM19A5-LRRC4B complex. Input paired multiple sequence alignments (paired MSAs) were generated following RoseTTAFold's input generation protocol. hMSAs for the FAM19A5 protein and LRRC4B extracellular domain were generated by an iterative sequence search against the UniClust30 database (*43*) using HHblits (*44*). To predict a complex structure, we generated a paired MSA based on individual MSA by pairing sequences from the same species. To provide pseudomultimer inputs to AlphaFold2, we used a gap insertion trick that has been previously applied to RoseTTAFold (*23*). The final models were ranked by predicted TM score (pTM score), and the best scored model was used for further study after structural relaxation using Rosetta (*22*). To identify the salt bridge, PyMOL (Schrödinger, LLC) was used to identify the charged

residues from the FAM19A5-LRRC4B complex. Then, atomic bonds between oxygen and nitrogen within 2.5 - 4.0 Å were screened.

In silico residue scanning of the FAM19A5-FB complex

We used the residue scanning module (Schrodinger Bioluminate®) for in silico residue scanning (e.g., Ala scanning) and to calculate the perturbation of protein-protein binding affinity, which was defined as the binding free energy change. To evaluate the potential impact of a mutation, we used Δ Affinity and Δ Stability (solvated) values.

Primary neuronal culture

Primary cortical or hippocampal neurons were prepared from postnatal C57BL/6 pups (Nara Biotech) at postnatal day 1 following established procedures (*45*). Initially, the cortices were dissected in Hank's buffered salt solution (HBSS) (Invitrogen) and then subjected to digestion with 2.5% trypsin for 15 minutes at 37°C. After this step, the supernatant was removed, and the tissues were washed with HBSS. The tissues were gently triturated, and the dissociated cells were plated on glass coverslips that were pre-coated with poly-D-lysine (in borate buffer at a concentration of 50 µg/ml, Sigma). These plated cells were housed in 60 mm culture dishes and cultured in minimum Eagle's medium (MEM) supplemented with 0.5% glucose, 1 mM pyruvate, 1.2 mM L-glutamine, and 12% fetal bovine serum. After 6 hours of incubation, the medium was replaced with neurobasal media (Invitrogen, Carlsbad, CA, USA) supplemented with 2% B-27 and 0.5 mM L-glutamine (Gibco). The cells were then maintained in a 5% CO_2-humidified incubator at 37°C. Every 3–4 days, half of the medium in the culture dish was replaced with fresh culture medium.

For RNA-seq analysis, neurons were cultured for DIV16, and total RNA was isolated at various time points: DIV 1, 3, 7, 10, and 16. This RNA was then subjected to RNA-seq analysis following established protocols (*46*).

Immunocytochemistry and immunohistochemistry

To conduct immunocytochemistry on HEK293 cells, we began by seeding the cells onto fibronectin-coated plastic film coverslips in 12-well plates at a density of 3×10^4 cells per well. After a 24-hour incubation period, these cells were co-transfected with 150 ng of FLAG-tagged LRRC4B and FAM19A5. Following another 24-hour incubation, we washed the cells once with ice-cold DPBS and then fixed them using 4% paraformaldehyde (PFA) in PBS for 20 minutes. After three subsequent washes with ice-cold DPBS, we blocked the cells using a buffer containing 3% bovine serum albumin (BSA) and 0.1% Triton X-100 in PBS for 30 minutes. The cells were then exposed to primary antibodies overnight at 4°C. After three more washes with DPBS, the cells underwent incubation with secondary antibodies and 20 mM Hoechst solution (Invitrogen) for 1 hour at room temperature. Following three final DPBS washes, we captured fluorescence images using a confocal microscope (Leica), and the coverslips were mounted with mounting solution (Biomeda). All images were processed using Las X software (Leica). It is important to note that NS101 and recombinant proteins containing the FB domain were treated for 30 minutes prior to fixation. Quantification of synaptic markers and their colocalization was performed using ImageJ (NIH) with the colocalization plugin.

Immunocytochemistry for Primary Cultured Neurons: For primary cultured neurons, fixation was carried out with 4% PFA, except for the spine density assay, which used a solution of 2% PFA and 4% sucrose. To quantify pre- and postsynaptic molecules, cultured neurons were treated with FAM19A5, FB proteins, hIgG, or NS101 at DIV 3 and DIV 6. At DIV 7, neurons were fixed and immunostained with anti-SYP (Sigma) and anti-PSD95 (Invitrogen). The detailed process was carried out as described above.

Immunohistochemistry for the brain slice: In the context of immunohistochemistry, mice underwent transcardial perfusion with a solution of 4% PFA in PBS, and their isolated brains were subsequently postfixed in the same fixative for a duration of 24 hours. These brains were then cryoprotected in 30% sucrose, serially sectioned on a cryostat (40 mm), and stored in a mixture of 50% glycerol and 50% PBS at −20°C until further use. Brain sections were blocked for 30 minutes in a buffer composed of 3% BSA and 0.1% Triton X-100 in PBS. They were then incubated with primary antibodies diluted in blocking buffer overnight at 4°C. After this overnight incubation, sections were subjected to three PBS washes and then incubated with secondary antibodies or Hoechst 33242 diluted in PBS for 30 minutes at room temperature. Subsequently, the sections were washed again, mounted, and observed either using a slide scanner (Zeiss) or a confocal microscope (Leica).

DiI staining and spine density analysis in vitro

To visualize dendritic spines, we used the well-characterized fluorescent lipophilic dye DiI (Invitrogen) according to the manufacturer's instructions. Primary neurons were treated with 10 nM hIgG or NS101 every 3 days starting at DIV 3. At DIV 15, primary neurons were fixed with 2% PFA + 4% sucrose in PBS for 15 min at room temperature and washed three times with DPBS. The cells were incubated with DiI solution diluted in DPBS (5 μl/ml) for 20 min at room temperature and washed three times with DPBS. After labeling, the coverslips incubated in DPBS were stored in the dark overnight at 4°C to allow DiI dye to diffuse. The following day, the coverslips were rinsed twice with 3' distilled water to reduce the background. The coverslips were mounted on slides using Crystal Mount (Biomeda) and cured for at least 2 days to allow complete migration of the dye into the spines. Serial Z-stacks (0.2 μm intervals) were performed using a 63x immersion lens. The 3D reconstruction of stacked images and analysis were performed using Imaris software, and the analysis was blinded. A protrusion width greater than 0.2 μm was defined as a dendritic spine.

Golgi staining

Golgi staining was performed according to the manufacturer's instructions (FD NeuroTechnologies, PK401). Whole fresh brains were collected and placed in the impregnation solution. The solution was replaced after 24 h, and then the brains were incubated at room temperature in the dark for 2 weeks, with gentle shaking every 3 days to prevent precipitation of the impregnation chemicals. After the impregnation step, the brains were placed in a rehydration solution for 1 week. The brains were frozen in a container with dry-ice cooled isopentane (Sigma-Aldrich, M32631) and cryosectioned into 100 μm slices. Prefrontal cortex slices were mounted on gelatin-coated slides (FD NeuroTechnolgies, PO101). For the developing step, the slides were placed for 10 min in the staining solution. The slides were dehydrated with increasing concentrations of pure ethanol (Sigma-Aldrich, E7023), cleared

with xylene (Daejung, 8587-4400), and then coverslipped with mounting medium (Sigma-Aldrich, 03989).

Confocal imaging and counting of dendritic spines

Dendritic spines were imaged from layer II/III of the prefrontal cortex using a 63x oil-immersion lens with 3x digital zoom. Basal dendrite 30 µm segments were sampled midway between the soma and the distal termination (medial). A total of 160 images were obtained from the brain section (80-µm thickness with 0.5 µm interval). Maximum intensity projection (MIP) images were obtained from a total of 160 images and processed with ImageJ software (NIH). 5 MIP images per subject were selected for quantification. The dendritic spine counter in ImageJ was used for dendritic spine counting and spine classification. At least 15 dendrites per subject were measured, and spines were classified as mushroom, stubby, thin, and filopodium using the criteria (*47*, *48*).

Hippocampal slice preparation and electrophysiology

APP/PS1 mice and WT mice (13 months old) were anesthetized with isoflurane (5% isoflurane, 95% O_2) and perfused with ice-cold sucrose artificial cerebrospinal fluid (aCSF) containing 195.5 mM sucrose, 2.5 mM KCl, 1 mM $NaH2PO_4$, 32.5 mM $NaHCO_3$, 11 mM glucose, 2 mM Na pyruvate, and 1 mM Na ascorbate (all chemicals from Sigma) bubbled with 95% O_2/5% CO_2 at a pH of 7.4. After perfusion, the brains were quickly removed from the skull, and sagittal hippocampal slices (400 µm thick) were cut on a vibratome (Leica). The slices were incubated at 35°C for 15 min in an incubation solution containing 119 mM NaCl, 2.5 mM KCl, 1 mM $NaH2PO_4$, 26.2 $NaHCO_3$, 11 mM glucose, 2 mM Na pyruvate, 1 mM Na ascorbate, 3 mM $MgSO_4$, and 1.5 mM $CaCl_2$. After incubation, the slices were transferred to aCSF solution at 23–24°C for 1 hour.

Field recordings were made with a concentric bipolar electrode positioned in the stratum radiatum of the CA1 region using an extracellular glass pipette (3–5 MΩ) filled with aCSF. Stimulation was delivered through a bipolar electrode (FHC, Bowdoin, ME, USA) placed in the SC-CA1. The SC circuit was visualized using differential interference contrast (DIC) microscopy at 4× magnification and identified by the ability to evoke short and constant latency fEPSPs at CA1 synapses by SC input stimulation. The test stimulation in all fEPSP experiments was measured before the experiments (30–300 µA), and a test-pulse stimulation strength that evoked 50% of the maximum fEPSP was used. Baseline synaptic responses were recorded for 30 min, and then LTP was induced by theta burst stimulation (100 Hz, 10 trains, 40 ms duration, 200 ms intertrain interval). LTP was calculated by an average of fEPSP amplitudes during the last 5 min of recordings. Recordings were made every 10 s for 1 hour using an Axopatch 700A amplifier (Molecular Devices) digitized at 10 kHz and filtered at two kHz with Digidata 1440A and pClamp 10.0 software (Molecular Devise).

To measure mEPSCs, the electrode was filled with an internal solution containing 135 mM Cs methane sulfonate, 8 mM NaCl, 10 mM HEPES, 0.5 mM EGTA, 4 mM Mg-ATP, 0.3 mM Na-GTP, and 5 mM QX-315 Cl; pH 7.25 with CsOH, 285 mOsm). Miniature currents were recorded in the presence of tetrodotoxin (1 µM TTX, Tocris) to block sodium currents and propagate action potentials.

Two-photon live imaging

Thirty-two female P301S mice (B6;C3-Tg (Prnp-MAPT*P301S) PS19Vle/J; JAX Strain #008169), as well as sixteen female B6C3F1/J (JAX Strain #100010) mice, were anesthetized with ketamine/xylazine and operated on for implantation of a cranial window (*49*). Before the surgery, mice received carprofen (subcutaneous, 5 mg/kg) to relieve pain during and after the surgery and dexamethasone (subcutaneous, 2 μg/g) to reduce inflammation. The cranial window was inserted over the somatosensory cortex at the following coordinates: AP −1.8, ML −2.0 from bregma. A dental drill (HP4–917, Foredom) was used to remove a round-shaped (d = 4 mm) piece of skull, and the hole in the bone was covered with a round cover glass (d = 5 mm; Electron Microscopy Sciences, 72296–05). A helicopter-shaped head plate (model 1; Neurotar) was placed over the cover glass and fixed with dental cement (Rapid Repair; Dentsply) mixed with cyanoacrylate glue (Loctite 401; Henkel) to a skull surface. An AAV viral vector encoding GFP under the control of the synapsin promoter (AAV-synapsin-GFP (AAV serotype 9); Signagen, SL100845-Std) was injected intracortically during the surgery (300 nanoliters, titer 1:10, depth of injection 800-900 micrometers from cortical surface) at the following coordinates: AP −1.8, ML −2.0 from bregma to fluorescently labeled neurons. Out of forty-eight operated mice, thirty mice with the most transparent cranial windows were selected for the imaging part of the study three weeks after implantation. The fourth week after surgery was dedicated to the habituation of mice to head fixation during four days of training. Therefore, imaging started after 4 weeks of post-surgical recovery. Each of these thirty mice was imaged seven times.

Mice were imaged with a FV1200MPE two-photon microscope (Olympus, Japan) with a 25X water immersion 1.05 NA objective specially designed for in vivo two-photon imaging. A MaiTai Broad Band DeepSee laser tuned to 900 nm was used for excitation. Emission light was collected using a bandpass filter (515–560 nm). For in vivo imaging sessions, awake animals were head-fixed under a two-photon microscope using the Mobile Home Cage device (Neurotar, Finland). The week prior to the start of imaging, animals were habituated to head fixation for four days.

After image acquisition, images were processed and analyzed using ImageJ (NIH). First, shifts between time points in the x, y, and z directions were compensated using Neurotar's scripts in ImageJ. Spine turnover analysis was performed by a scientist completely blinded to the identity of the treatment groups. Individual spines were tracked manually by visual identification in the 3D stacks of images collected at all time points. Protrusions of at least 5 pixels from the dendritic shaft were considered candidate spines. After identification of a candidate spine, the data analyst examined 10 adjacent slices in both directions looking for other explanations for the protrusion. If no other explanation was found, the spine was counted in the analysis. At every time point, each spine was assigned a specific code, either 1 (present) or 0 (absent). If, in some instances, the image quality was not sufficiently sharp for spine identification at a specific time point, the spine was assigned a code -1 and excluded from further analysis.

Stereotaxic FAM19A5 injection

For stereotaxic injection of WT and MT FAM19A5(R58A, R59A), 3-month-old male and female mice were anesthetized with xylazine and ketamine. An injection cannula was inserted stereotaxically into the striatum (mediolateral, 2.0 mm from bregma; anteroposterior, 0.5 mm; dorsoventral, 3.5 mm) unilaterally (inserted into the right hemisphere). The infusion was performed at a rate of 0.2 μl per min, and 2 μl of FAM19A5 (diluted in PBS at a concentration of 5 μg/μl) or the same volume of PBS was injected into the mouse.

Animal behavioral tests

Male mice used in all behavioral tests were 9–11 months old. All assays used littermates or age-matched animals. Behavioral tests were performed in a light- and noise-controlled behavioral room, where the animals were allowed to adapt for one hour before each behavioral test. All behavioral results were analyzed blindly.

Y-maze test

A Y-shaped maze consists of three identical arms (40 cm in length, 15 cm in height) at a 120° angle from each other. Mice were allowed to freely explore the three arms for 8 min with a luminosity of 40 lux. The sequence and the total number of arms entered were measured. Spontaneous alteration (%) was calculated as follows: the number of triads containing entries into all three arms/maximum possible alternations (the total number of arms entered – 2) × 100. Mice that constituted fewer than 10 of the total arm entries were omitted from the analysis.

Morris water maze test

Mice were trained to find the hidden platform (9 cm in diameter) in a stainless-steel pool (90 cm in diameter, 50 cm in height) filled with water (22 ± 1°C) to a depth of 30 cm. The platform was 1 cm below the water level. In the acquisition phase, mice were trained for six consecutive days with four trials/per day. Each trial ended either when an animal climbed onto the platform or when a maximum of 60 s had elapsed. Next, mice were allowed to remain on the platform for 10 s. If they failed to locate the platform within 60 s, they were guided to the platform and left there for 10 s, and the escape time was recorded as 60 s. On day 7, for the probe test, the platform was removed, and mice were allowed to explore freely for 60 s. The spatial memory ability of individual animals in the probe test was determined by the following parameters: latency to target, target crossing number, distance to the target, percentage in quadrant SW, and percentage in the target. Target and quadrant SW refer to the location and quadrant where the hidden platform was located, respectively. These parameters were analyzed by SMART video tracking software (Panlab). Mice displaying abnormal behaviors, such as freezing and floating, were excluded from the final data.

Passive avoidance test

The passive avoidance test, performed in plastic cages of identical size, assessed associative learning and memory by using the rodents' innate preference for darkness. The inside of a darkened cage was designed to induce a foot shock; thus, when mice entered the dark compartment from the light compartment, a foot shock (0.5 mA intensity) was delivered for 3 s. To assess memory, we placed mice in the light compartment 24 hours later and measured the time it took to enter the dark compartment. The maximal latency was 300 s. Animals showing freezing behaviors (with acquisition time ≥ 200 s) or abnormal exploration were excluded from the final analysis.

Quantification and statistical analysis

All statistical analyses were performed using GraphPad Prism 8 with 95% confidence. All data are presented as the mean ± SEM. All the details of the statistical tests and results are reported in the figure legends.

References and Notes

1. O. Palasca, A. Santos, C. Stolte, J. Gorodkin, L. J. Jensen, TISSUES 2.0: an integrative web resource on mammalian tissue expression. *Database (Oxford)*. **2018**, bay003 (2018). doi:10.1093/database/bay028
2. Y. Tom Tang, P. Emtage, W. D. Funk, T. Hu, M. Arterburn, E. E. J. Park, F. Rupp, TAFA: a novel secreted family with conserved cysteine residues and restricted expression in the brain. *Genomics*. **83**, 727–734 (2004). doi:10.1016/j.ygeno.2003.10.006
3. I. Jeong, S. Yun, A. Shahapal, E. B. Cho, S. W. Hwang, J. Y. Seong, H.-C. Park, FAM19A5l affects mustard oil-induced peripheral nociception in zebrafish. *Mol Neurobiol*. **58**, 4770–4785 (2021). doi:10.1007/s12035-021-02449-z
4. J. Mez, J. Chung, G. Jun, J. Kriegel, A. P. Bourlas, R. Sherva, M. W. Logue, L. L. Barnes, D. A. Bennett, J. D. Buxbaum, G. S. Byrd, P. K. Crane, N. Ertekin-Taner, D. Evans, M. D. Fallin, T. Foroud, A. Goate, N. R. Graff-Radford, K. S. Hall, M. I. Kamboh, W. A. Kukull, E. B. Larson, J. J. Manly, Alzheimer's Disease Genetics Consortium, J. L. Haines, R. Mayeux, M. A. Pericak-Vance, G. D. Schellenberg, K. L. Lunetta, L. A. Farrer, Two novel loci, COBL and SLC10A2, for Alzheimer's disease in African Americans. *Alzheimers Dement*. **13**, 119–129 (2017). doi:10.1016/j.jalz.2016.09.002
5. A. A. Kashevarova, E. O. Belyaeva, A. M. Nikonov, O. V. Plotnikova, N. A. Skryabin, T. V. Nikitina, S. A. Vasilyev, Y. S. Yakovleva, N. P. Babushkina, E. N. Tolmacheva, M. E. Lopatkina, R. R. Savchenko, L. P. Nazarenko, I. N. Lebedev, Compound phenotype in a girl with r(22), concomitant microdeletion 22q13.32-q13.33 and mosaic monosomy 22. *Mol Cytogenet*. **11**, 26 (2018). doi:10.1186/s13039-018-0375-3
6. S. Huang, C. Zheng, G. Xie, Z. Song, P. Wang, Y. Bai, D. Chen, Y. Zhang, P. Lv, W. Liang, S. She, Q. Li, Z. Liu, Y. Wang, G.-G. Xing, Y. Wang, FAM19A5/TAFA5, a novel neurokine, plays a crucial role in depressive-like and spatial memory-related behaviors in mice. *Mol Psychiatry*. **26**, 2363–2379 (2021). doi:10.1038/s41380-020-0720-x
7. D. C. Sarver, X. Lei, G. W. Wong, FAM19A (TAFA): An Emerging family of neurokines with diverse functions in the central and peripheral nervous system. *ACS Chem Neurosci.* **12**, 945–958 (2021). doi:10.1021/acschemneuro.0c00757
8. A. J. Khalaj, F. H. Sterky, A. Sclip, J. Schwenk, A. T. Brunger, B. Fakler, T. C. Südhof, Deorphanizing FAM19A proteins as pan-neurexin ligands with an unusual biosynthetic binding mechanism. *J Cell Biol*. **219**, e202004164 (2020). doi:10.1083/jcb.202004164
9. Y. Zhang, H. Chen, R. Li, K. Sterling, W. Song, Amyloid β-based therapy for Alzheimer's disease: challenges, successes and future. *Signal Transduct Target Ther*. **8**, 1–26 (2023). doi:10.1038/s41392-023-01484-7
10. C. H. van Dyck, C. J. Swanson, P. Aisen, R. J. Bateman, C. Chen, M. Gee, M. Kanekiyo, D. Li, L. Reyderman, S. Cohen, L. Froelich, S. Katayama, M. Sabbagh, B. Vellas, D. Watson, S. Dhadda, M. Irizarry, L. D. Kramer, T. Iwatsubo, Lecanemab in early Alzheimer's disease. *N Engl J Med*. **388**, 9–21 (2023). doi:10.1056/NEJMoa2212948
11. J. Sevigny, P. Chiao, T. Bussière, P. H. Weinreb, L. Williams, M. Maier, R. Dunstan, S. Salloway, T. Chen, Y. Ling, J. O'Gorman, F. Qian, M. Arastu, M. Li, S. Chollate, M. S. Brennan, O. Quintero-Monzon, R. H. Scannevin, H. M. Arnold, T. Engber, K. Rhodes, J.

Ferrero, Y. Hang, A. Mikulskis, J. Grimm, C. Hock, R. M. Nitsch, A. Sandrock, The antibody aducanumab reduces Aβ plaques in Alzheimer's disease. *Nature*. **537**, 50–56 (2016). doi:10.1038/nature19323
12. A. Mullard, FDA approval for Biogen's aducanumab sparks Alzheimer disease firestorm. *Nat Rev Drug Discov*. **20**, 496 (2021). doi:10.1038/d41573-021-00099-3
13. D. S. Knopman, D. T. Jones, M. D. Greicius, Failure to demonstrate efficacy of aducanumab: An analysis of the EMERGE and ENGAGE trials as reported by Biogen, December 2019. *Alzheimers Dement*. **17**, 696–701 (2021). doi:10.1002/alz.12213
14. M. Tzioras, R. I. McGeachan, C. S. Durrant, T. L. Spires-Jones, Synaptic degeneration in Alzheimer disease. *Nat Rev Neurol*. **19**, 19–38 (2023). doi:10.1038/s41582-022-00749-z
15. B. Lu, G. Nagappan, X. Guan, P. J. Nathan, P. Wren, BDNF-based synaptic repair as a disease-modifying strategy for neurodegenerative diseases. *Nat Rev Neurosci*. **14**, 401–416 (2013). doi:10.1038/nrn3505
16. J. Jackson, E. Jambrina, J. Li, H. Marston, F. Menzies, K. Phillips, G. Gilmour, Targeting the synapse in Alzheimer's disease. *Front Neurosci*. **13**, 735 (2019). doi:10.3389/fnins.2019.00735
17. A. Zeisel, H. Hochgerner, P. Lönnerberg, A. Johnsson, F. Memic, J. van der Zwan, M. Häring, E. Braun, L. E. Borm, G. L. Manno, S. Codeluppi, A. Furlan, K. Lee, N. Skene, K. D. Harris, J. Hjerling-Leffler, E. Arenas, P. Ernfors, U. Marklund, S. Linnarsson, Molecular architecture of the mouse nervous system. *Cell*. **174**, 999-1014.e22 (2018). doi:10.1016/j.cell.2018.06.021
18. H. Wang, K. K. Dey, P.-C. Chen, Y. Li, M. Niu, J.-H. Cho, X. Wang, B. Bai, Y. Jiao, S. R. Chepyala, V. Haroutunian, B. Zhang, T. G. Beach, J. Peng, Integrated analysis of ultra-deep proteomes in cortex, cerebrospinal fluid and serum reveals a mitochondrial signature in Alzheimer's disease. *Mol Neurodegener*. **15**, 43 (2020). doi:10.1186/s13024-020-00384-6
19. L.-L. Xiong, L.-L. Xue, Y.-J. Chen, R.-L. Du, Q. Wang, S. Wen, L. Zhou, T. Liu, T.-H. Wang, C.-Y. Yu, Proteomics study on the cerebrospinal fluid of patients with encephalitis. *ACS Omega*. **6**, 16288–16296 (2021). doi:10.1021/acsomega.1c00367
20. S. Westwood, B. Liu, A. L. Baird, S. Anand, A. J. Nevado-Holgado, D. Newby, M. Pikkarainen, M. Hallikainen, J. Kuusisto, J. R. Streffer, G. Novak, K. Blennow, U. Andreasson, H. Zetterberg, U. Smith, M. Laakso, H. Soininen, S. Lovestone, The influence of insulin resistance on cerebrospinal fluid and plasma biomarkers of Alzheimer's pathology. *Alzheimers Res Ther*. **9**, 31 (2017). doi:10.1186/s13195-017-0258-6
21. K. Suzuki, J. Elegheert, I. Song, H. Sasakura, O. Senkov, K. Matsuda, W. Kakegawa, A. J. Clayton, V. T. Chang, M. Ferrer-Ferrer, E. Miura, R. Kaushik, M. Ikeno, Y. Morioka, Y. Takeuchi, T. Shimada, S. Otsuka, S. Stoyanov, M. Watanabe, K. Takeuchi, A. Dityatev, A. R. Aricescu, M. Yuzaki, A synthetic synaptic organizer protein restores glutamatergic neuronal circuits. *Science*. **369**, eabb4853 (2020). doi:10.1126/science.abb4853
22. I. R. Humphreys, J. Pei, M. Baek, A. Krishnakumar, I. Anishchenko, S. Ovchinnikov, J. Zhang, T. J. Ness, S. Banjade, S. R. Bagde, V. G. Stancheva, X.-H. Li, K. Liu, Z. Zheng, D. J. Barrero, U. Roy, J. Kuper, I. S. Fernández, B. Szakal, D. Branzei, J. Rizo, C. Kisker, E. C. Greene, S. Biggins, S. Keeney, E. A. Miller, J. C. Fromme, T. L. Hendrickson, Q. Cong, D. Baker, Computed structures of core eukaryotic protein complexes. *Science*. **374**, eabm4805 (2021). doi:0.1126/science.abm4805
23. M. Baek, F. DiMaio, I. Anishchenko, J. Dauparas, S. Ovchinnikov, G. R. Lee, J. Wang, Q. Cong, L. N. Kinch, R. D. Schaeffer, C. Millán, H. Park, C. Adams, C. R. Glassman, A. DeGiovanni, J. H. Pereira, A. V. Rodrigues, A. A. van Dijk, A. C. Ebrecht, D. J. Opperman, T. Sagmeister, C. Buhlheller, T. Pavkov-Keller, M. K. Rathinaswamy, U. Dalwadi, C. K. Yip, J. E. Burke, K. C. Garcia, N. V. Grishin, P. D. Adams, R. J. Read, D. Baker, Accurate prediction

of protein structures and interactions using a three-track neural network. *Science*. **373**, 871–876 (2021). doi:10.1126/science.abj8754
24. J. Jumper, R. Evans, A. Pritzel, T. Green, M. Figurnov, O. Ronneberger, K. Tunyasuvunakool, R. Bates, A. Žídek, A. Potapenko, A. Bridgland, C. Meyer, S. A. A. Kohl, A. J. Ballard, A. Cowie, B. Romera-Paredes, S. Nikolov, R. Jain, J. Adler, T. Back, S. Petersen, D. Reiman, E. Clancy, M. Zielinski, M. Steinegger, M. Pacholska, T. Berghammer, S. Bodenstein, D. Silver, O. Vinyals, A. W. Senior, K. Kavukcuoglu, P. Kohli, D. Hassabis, Highly accurate protein structure prediction with AlphaFold. *Nature*. **596**, 583–589 (2021). doi:10.1038/s41586-021-03819-2
25. J. Woo, S.-K. Kwon, S. Choi, S. Kim, J.-R. Lee, A. W. Dunah, M. Sheng, E. Kim, Trans-synaptic adhesion between NGL-3 and LAR regulates the formation of excitatory synapses. *Nat Neurosci*. **12**, 428–437 (2009). doi:10.1038/nn.2279
26. Y. J. Yu, R. J. Watts, Developing therapeutic antibodies for neurodegenerative disease. *Neurotherapeutics*. **10**, 459–472 (2013). doi:10.1007/s13311-013-0187-4
27. J. H. Morrison, M. G. Baxter, The aging cortical synapse: hallmarks and implications for cognitive decline. *Nat Rev Neurosci*. **13**, 240–250 (2012). doi:10.1038/nrn3200
28. D. J. Selkoe, Alzheimer's disease is a synaptic failure. *Science*. **298**, 789–791 (2002). doi:10.1126/science.1074069
29. E. E. Congdon, E. M. Sigurdsson, Tau-targeting therapies for Alzheimer disease. *Nat Rev Neurol*. **14**, 399–415 (2018). doi:10.1038/s41582-018-0013-z
30. Y. Yoshiyama, M. Higuchi, B. Zhang, S.-M. Huang, N. Iwata, T. C. Saido, J. Maeda, T. Suhara, J. Q. Trojanowski, V. M.-Y. Lee, Synapse loss and microglial activation precede tangles in a P301S tauopathy mouse model. *Neuron*. **53**, 337–351 (2007). doi:10.1016/j.neuron.2007.01.010
31. C. K. Walker, K. M. Greathouse, B. D. Boros, E. H. Poovey, K. R. Clearman, R. Ramdas, H. M. Muhammad, J. H. Herskowitz, Dendritic spine remodeling and synaptic Tau levels in PS19 tauopathy mice. *Neuroscience*. **455**, 195–211 (2021). doi:10.1016/j.neuroscience.2020.12.006
32. C. S. Bold, D. Baltissen, S. Ludewig, M. K. Back, J. Just, L. Kilian, S. Erdinger, M. Banicevic, L. Rehra, F. Almouhanna, M. Nigri, D. P. Wolfer, R. Spilger, K. Rohr, O. Kann, C. J. Buchholz, J. von Engelhardt, M. Korte, U. C. Müller, APPsα rescues Tau-induced synaptic pathology. *J Neurosci.* **42**, 5782–5802 (2022). doi:10.1523/JNEUROSCI.2200-21.2022
33. A. K. McAllister, Dynamic aspects of CNS synapse formation. *Annu Rev Neurosci*. **30**, 425–450 (2007). doi:10.1146/annurev.neuro.29.051605.112830
34. M. Abitz, R. D. Nielsen, E. G. Jones, H. Laursen, N. Graem, B. Pakkenberg, Excess of neurons in the human newborn mediodorsal thalamus compared with that of the adult. *Cereb Cortex*. **17**, 2573–2578 (2007). doi:10.1093/cercor/bhl163
35. S. W. Scheff, D. A. Price, F. A. Schmitt, E. J. Mufson, Hippocampal synaptic loss in early Alzheimer's disease and mild cognitive impairment. *Neurobiol Aging*. **27**, 1372–1384 (2006). doi:10.1016/j.neurobiolaging.2005.09.012
36. H. Mathys, J. Davila-Velderrain, Z. Peng, F. Gao, S. Mohammadi, J. Z. Young, M. Menon, L. He, F. Abdurrob, X. Jiang, A. J. Martorell, R. M. Ransohoff, B. P. Hafler, D. A. Bennett, M. Kellis, L.-H. Tsai, Single-cell transcriptomic analysis of Alzheimer's disease. *Nature*. **570**, 332–337 (2019). doi: 10.1038/s41586-019-1195-2
37. M. Otero-Garcia, S. U. Mahajani, D. Wakhloo, W. Tang, Y.-Q. Xue, S. Morabito, J. Pan, J. Oberhauser, A. E. Madira, T. Shakouri, Y. Deng, T. Allison, Z. He, W. E. Lowry, R. Kawaguchi, V. Swarup, I. Cobos, Molecular signatures underlying neurofibrillary tangle susceptibility in Alzheimer's disease. *Neuron*. **110**, 2929-2948.e8 (2022). doi:10.1016/j.neuron.2022.06.021

38. B. P. Imbimbo, C. Balducci, S. Ippati, M. Watling, Initial failures of anti-tau antibodies in Alzheimer's disease are reminiscent of the amyloid-β story. *Neural Regen Res*. **18**, 117–118 (2023). doi:10.4103/1673-5374.340409
39. A. Mullard, Landmark Alzheimer's drug approval confounds research community. *Nature*. **594**, 309–310 (2021). doi: 10.1038/d41586-021-01546-2
40. S. Reardon, FDA approves Alzheimer's drug lecanemab amid safety concerns. *Nature*. **613**, 227–228 (2023). doi:10.1038/d41586-023-00030-3
41. M. Prillaman, Alzheimer's drug slows mental decline in trial - but is it a breakthrough? *Nature*. **610**, 15–16 (2022). doi:10.1038/d41586-022-03081-0
42. H. Kwak, E.-H. Cho, E. B. Cho, Y.-N. Lee, A. Shahapal, H. J. Yong, A. Reyes-Alcaraz, Y. Jeong, Y. Lee, M. Lee, N. Ha, S. Oh, J. K. Lee, W. S. Lee, W. Kim, J.-I. Hwang, J. Y. Seong, Is FAM19A5 an adipokine? Peripheral FAM19A5 in wild-type, FAM19A5 knock-out, and LacZ knock-in mice *bioRxiv* 2020.02. 19.955351. (2020) doi:10.1101/2020.02.19.955351.
43. M. Mirdita, L. von den Driesch, C. Galiez, M. J. Martin, J. Söding, M. Steinegger, Uniclust databases of clustered and deeply annotated protein sequences and alignments. *Nucleic Acids Res.* 45, D170–D176 (2017). doi:10.1093/nar/gkw1081
44. M. Remmert, A. Biegert, A. Hauser, J. Söding, HHblits: lightning-fast iterative protein sequence searching by HMM-HMM alignment. *Nat Methods.* 9, 173–175 (2012). doi:10.1038/nmeth.1818
45. G. M. J. Beaudoin, S.-H. Lee, D. Singh, Y. Yuan, Y.-G. Ng, L. F. Reichardt, J. Arikkath, Culturing pyramidal neurons from the early postnatal mouse hippocampus and cortex. *Nat Protoc.* 7, 1741–1754 (2012). doi:10.1038/nprot.2012.099
46. J. A. Martin, Z. Wang, Next-generation transcriptome assembly. *Nat Rev Genet.* 12, 671–682 (2011). doi:10.1038/nrg3068
47. T. Tanaka, Development of an efficient method for classifying large numbers of dendritic spines using confocal microscopy. *Juntendo Medical Journal.* 67, 329–332 (2021). doi:10.14789/jmj.JMJ21-R02
48. W. C. Risher, T. Ustunkaya, J. S. Alvarado, C. Eroglu, Rapid Golgi analysis method for efficient and unbiased classification of dendritic Spines. *PLoS One.* 9, e107591 (2014). doi:10.1371/journal.pone.0107591
49. E. Pryazhnikov, E. Mugantseva, P. Casarotto, J. Kolikova, S. M. Fred, D. Toptunov, R. Afzalov, P. Hotulainen, V. Voikar, R. Terry-Lorenzo, S. Engel, S. Kirov, E. Castren, L. Khiroug, Longitudinal two-photon imaging in somatosensory cortex of behaving mice reveals dendritic spine formation enhancement by subchronic administration of low-dose ketamine. *Sci. Rep.* 8, 6464 (2018). doi:10.1038/s41598-018-24933-8

Acknowledgments:

The authors acknowledge Eun Bee Cho, Yongwoo Jeong, and Sitaek Oh for assisting in manuscript preparation. The authors also acknowledge Richard Larouche and Hyun Jung Jung for organizing and conducting the clinical phase 1 trial. The authors also acknowledge Kyungho Seong for performing in silico residue scanning on the FAM19A5-FB complex using the Schrödinger Platform.

Funding: This work was supported by grants from Neuracle Science Co., Ltd.

Author contributions:

Conceptualization: JY.S, SJ.Y, HB.K, HY.K, SX.M, RH.K. Experiments: HB.K, HY.K, SX.M, MHL., N.H, EH.C, SM.L, JW.J, M.B, SI.P Analysis: SJ.Y., RH.K., HY.K., HB.K., SX.M.,

MH.L., N.H., EH.C., SM.L., M.B., SI.P., SG.K Investigation: SJ.Y, HB.K, RH.K, SX.M Resources: WK.K, JI.H Data curation: SJ. Y, RH.K, SX.M, HB.K, Writing: SJ. Y, JY. S, RH. K, SX.M, HB.K, HC.P, M.B, SW.H, JI.H. Visualization: SJ. Y, HB. K, RH. K, SX. M, JY.S. Supervision: JY.S. Project administration: JY.S. Funding acquisition: JY.S.

Competing interests:

HB.K, SJ.Y, HY.K, SX.M, RH.K, MH.L, N.H, EH.C, SM.L, JW.J, WK.K, YS.P, SI.P, SG.K and JY.S are employed by Neuracle Science, Co., Ltd. MH.L, SM.L, WK.K, SW.H, HC.P, and JY.S are shareholders of Neuracle Science, Co., Ltd. The remaining authors have no conflicts of interest to declare.

Data availability

HEK293 cells were obtained for research use through a materials transfer agreement with ATCC. Plasmids were obtained through a materials transfer agreement with Genscript. All mouse strains have been made publicly available through The Jackson Laboratory. Other materials are available under a materials transfer agreement for noncommercial replication or extension of this work upon request to the corresponding authors. All other information is available in the manuscript or the supplementary materials.

Figures

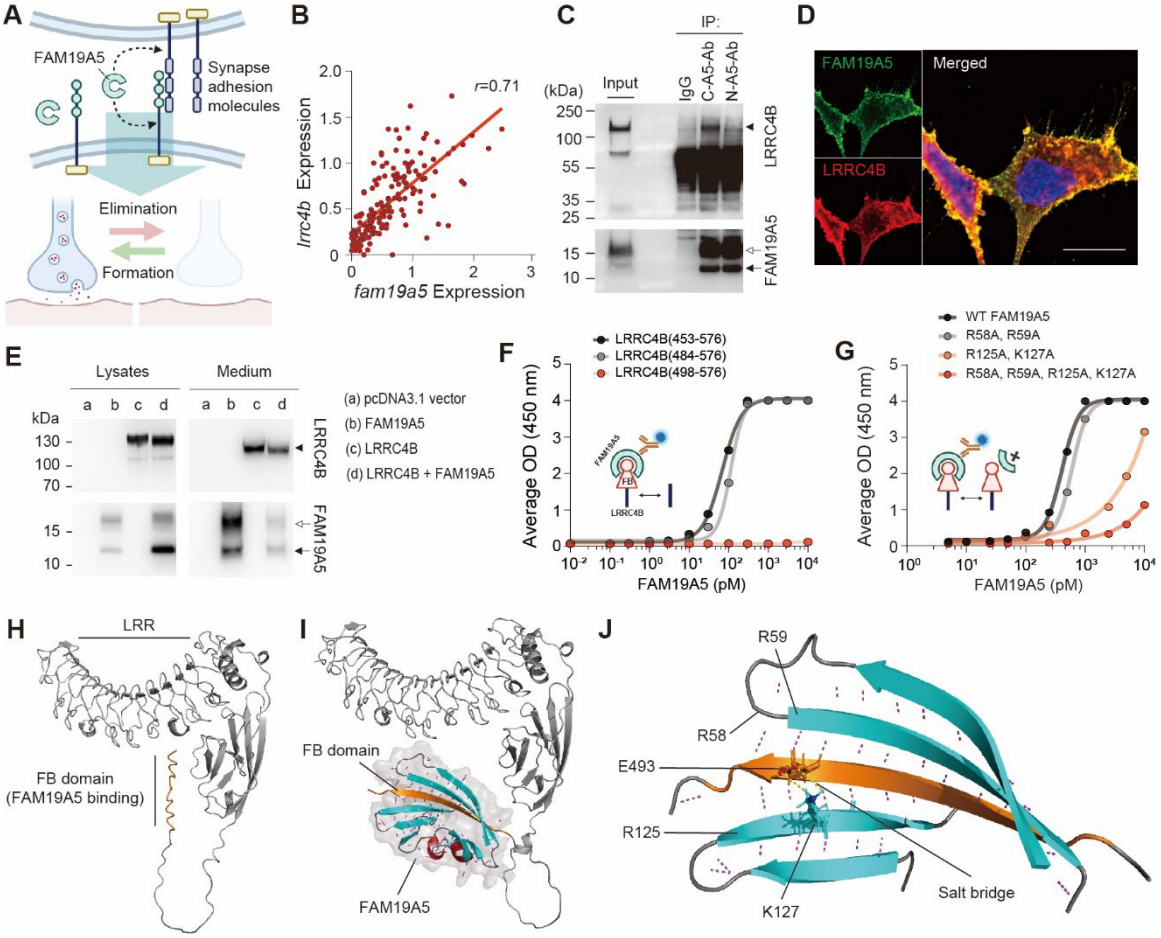

Figure 1. FAM19A5 binds to the FB domain of LRRC4B.

(A) Illustration of the potential mechanisms of synapse regulation. FAM19A5 binding to adhesion molecules could induce either synapse elimination or formation. (B) Correlation between the RNA transcript levels of *lrrc4b* and *fam19a5* in 168 neuron types. Correlation coefficient; $r = 0.71$, $P < 0.0001$. (C) Co-IP of human CSF using FAM19A5 antibodies (C-A5-Ab or N-A5-Ab). Solid arrowhead: LRRC4B, open arrow: glycosylated FAM19A5, solid arrow: non-glycosylated FAM19A5. (D) Representative ICC image of HEK293 cells co-expressing FAM19A5 (green) and FLAG-tagged LRRC4B (red). Nucleus (blue). Scale bar, 20 μm. (E) Immunoblots of LRRC4B and FAM19A5 in culture lysate and medium from HEK293 cells co-expressing LRRC4B and FAM19A5. Solid arrowhead: LRRC4B, open arrow: glycosylated FAM19A5, solid arrow: non-glycosylated FAM19A5. (F) The binding affinity of LRRC4B to FAM19A5 was determined via ELISA (inserted, captured by LRRC4B-hFc, detected by HRP-conjugated C-A5-Ab). EC_{50} of LRRC4B(453-576)-hFc = 68.5 pM, EC_{50} of LRRC4B(484-576)-hFc = 112.1 pM. (G) Binding affinity of wild-type (WT) or mutant (MT) FAM19A5 proteins (R58A, R59A; R125A, K127A; R58A, R59A, R125A, K127A) to LRRC4B measured via ELISA (inserted, captured by His-TEV LRRC4B, detected by HRP-conjugated C-A5-Ab). EC_{50} of WT FAM19A5 = 409.5 pM, EC_{50} of MT FAM19A5(R58A, R59A) = 594.8 pM. (H) *In silico* model of LRRC4B, including the leucine-rich repeat (LRR), immunoglobulin C (IgC), and FB domain (orange). (I) *In silico* model of the LRRC4B-FAM19A5 complex. The FAM19A5 structures (gray surface) are depicted as α-helices (red)

and β-strands (cyan). (J) Model showing the salt bridge between the side chains of E493 (orange) and K127 (cyan). Hydrogen bonds are represented by dashed lines. The predicted key residues of FAM19A5 for binding to the FB domain (484-498, orange) are R58, R59, R125, and K127.

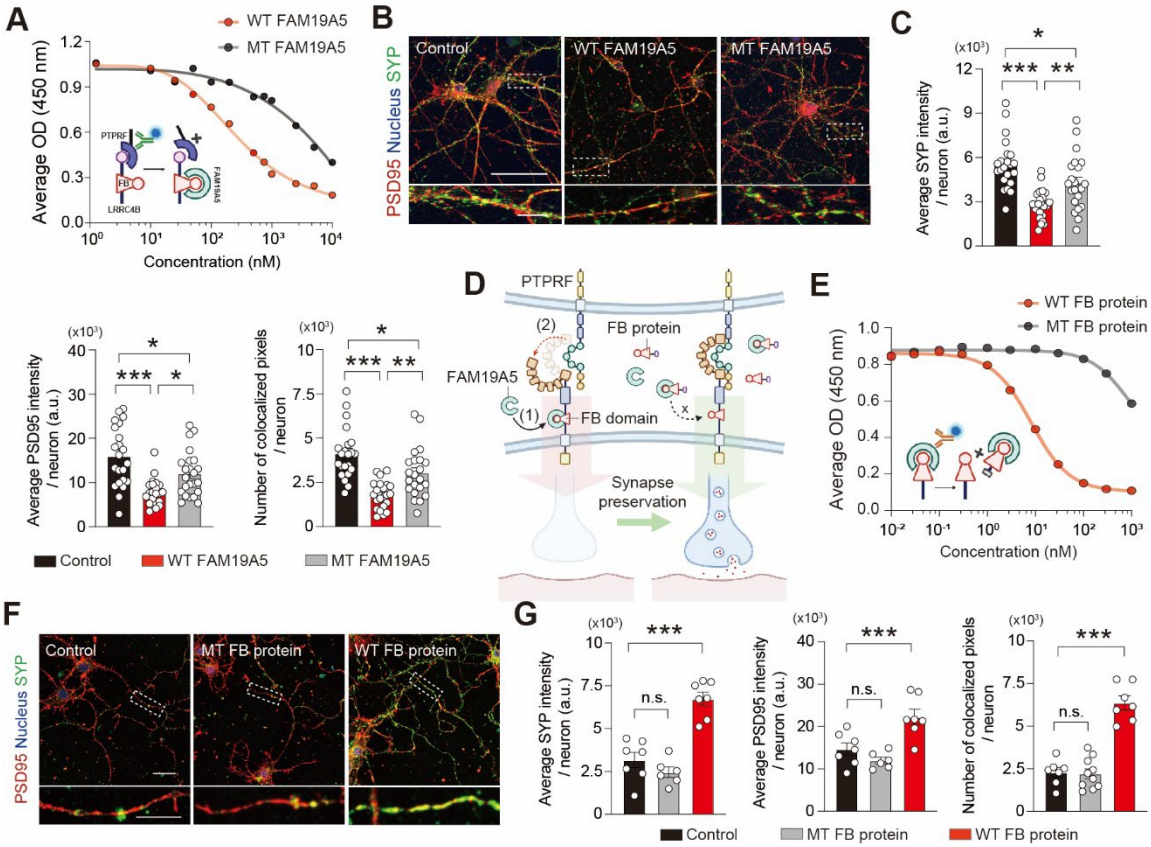

Figure 2. FAM19A5 binding to LRRC4B leads to the dissociation of synaptic contacts.

(A) Dissociation of the LRRC4B-PTPRF complex in the presence of WT FAM19A5 or MT FAM19A5(R58A, R59A, R125A, K127A) determined via ELISA (inserted, captured by His-TEV LRRC4B, detected by HRP-conjugated anti-human IgG Fc). IC_{50} of WT FAM19A5 = 281 nM. (B) Representative ICC image of cultured hippocampal neurons treated with 50 nM WT or MT FAM19A5(R58A, R59A, R125A, K127A) stained with pre-synaptic marker synaptophysin (SYP; green) and post-synaptic marker PSD95 (red). Nucleus (blue). Scale bar, 50 μm, 10 μm (enlarged). (C) Quantification of the intensity and colocalization of markers from (B) (n = 22 per group). (D) An illustration of how the FB-containing protein prevents synapse loss by inhibiting FAM19A5. (E) Inhibition of FAM19A5-LRRC4B binding by WT LRRC4B(453–576)-hFc or MT LRRC4B(453–576, T488A, T489A)-hFc FB proteins determined via ELISA (inserted, captured by LRRC4B(36-576)-hFc, detected by HRP-conjugated C-A5-Ab). IC_{50} of WT FB protein = 8.1 nM. (F) Representative ICC image of cultured hippocampal neurons treated with WT LRRC4B(453–576-hFc) or MT LRRC4B(453–576, T488A, T489A)-hFc FB proteins stained with SYP (green) and PSD95 (red). Nucleus (blue). Scale bar, 20 μm, 10 μm (enlarged). (G) Quantification of the intensity and colocalization of markers from (F) (n = 6 to 7 per group). Data are presented as the mean ± SEM. One-way ANOVA with Tukey's multiple comparisons test in (C) and (G) was used to calculate *P* values. n.s., not significant; *$P < 0.05$, **$P < 0.01$, ***$P < 0.001$.

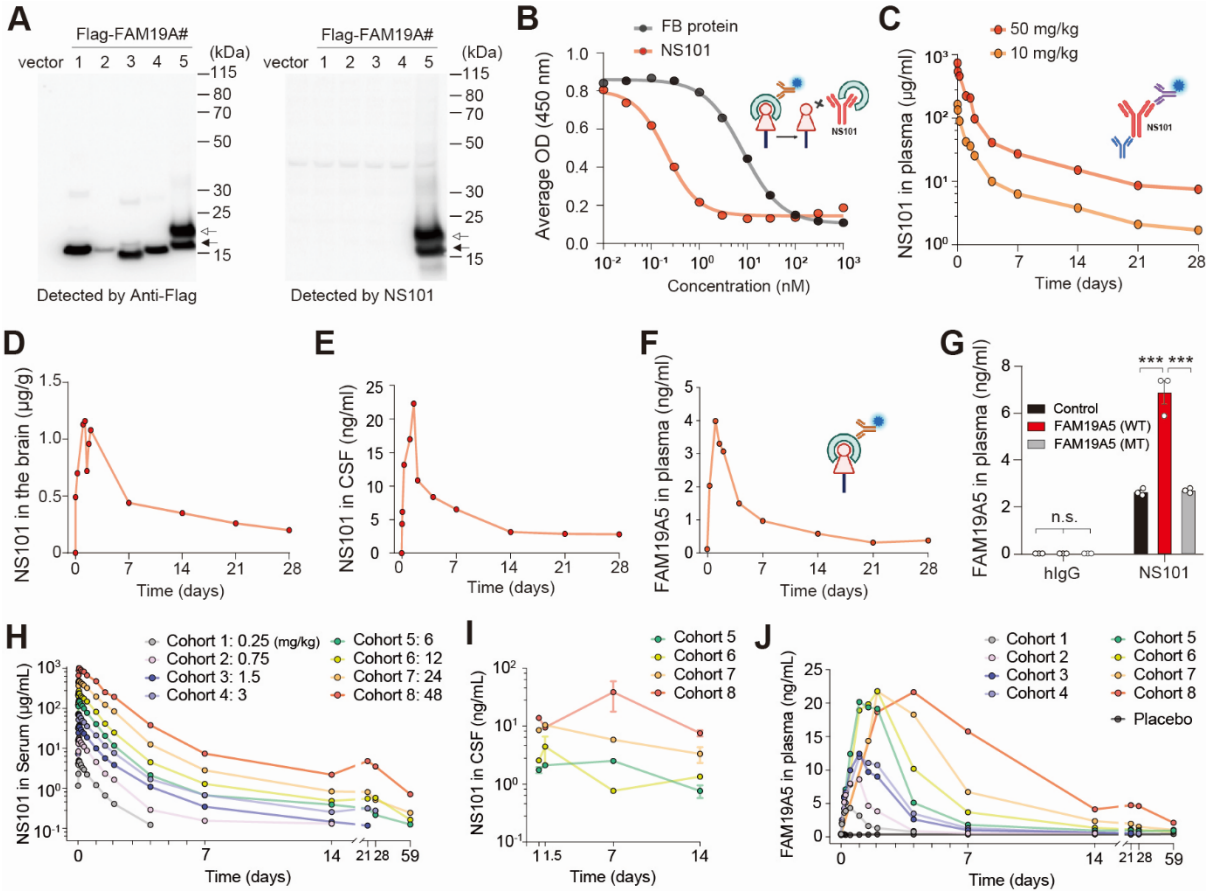

Figure 3. NS101, a potent monoclonal antibody against FAM19A5.

(A) Western blot analysis of FAM19A families (FAM19A#) detected by anti-Flag (left) and NS101 (right). (B) Inhibition efficacy of NS101 or FB protein on FAM19A5-LRRC4B binding determined via ELISA (inserted, captured by LRRC4B(36-576)-hFc, detected by HRP-conjugated C-A5-Ab). IC_{50} of NS101 = 205.0 pM, IC_{50} of FB protein = 8.1 nM. (C) Plasma NS101 levels at the indicated time points after a single IV administration of 10 mg/kg or 50 mg/kg NS101 determined via ELISA (inserted, captured by rabbit anti-human IgG Fc, detected by HRP-conjugated hIgG kappa light chain antibody). NS101 levels in the (D) mouse brain and (E) rat CSF at the indicated time points after a single IV administration of 10 mg/kg determined via ELISA (captured by rabbit anti-human IgG heavy chain, detected by HRP-conjugated hIgG kappa light chain antibody). (F) Brain-secreted FAM19A5 levels in rat blood plasma at the indicated time points after a single IV administration of 10 mg/kg NS101, determined via ELISA (inserted, captured by His-TEV hLRRC4B(453-576), detected by HRP-conjugated C-A5-Ab). (G) Plasma FAM19A5 levels after brain infusion of WT and MT FAM19A5(R58A, R59A). One day after the infusion, mice were IV administered with hIgG or 10 mg/kg NS101. ELISA was performed using His-TEV LRRC4B and HRP-conjugated SS01 (n = 3 per group). NS101 levels in (H) human serum and (I) human CSF at the indicated time points after a single IV administration of 0.25 to 48 mg/kg determined via ELISA (captured by N'HIS-TEV FAM19A5, rabbit anti-NS101, detected by sulfo-tag anti-rabbit antibody). (J) Brain-secreted FAM19A5 levels in human blood plasma at the indicated time points after the administrations determined by ELISA (captured by His-TEV LRRC4B,

detected by HRP-conjugated SS01). Data are presented as the mean ± SEM. One-way ANOVA followed by Tukey's multiple comparison test in (G) was used to calculate *P* values. n.s., not significant; ***$P < 0.001$.

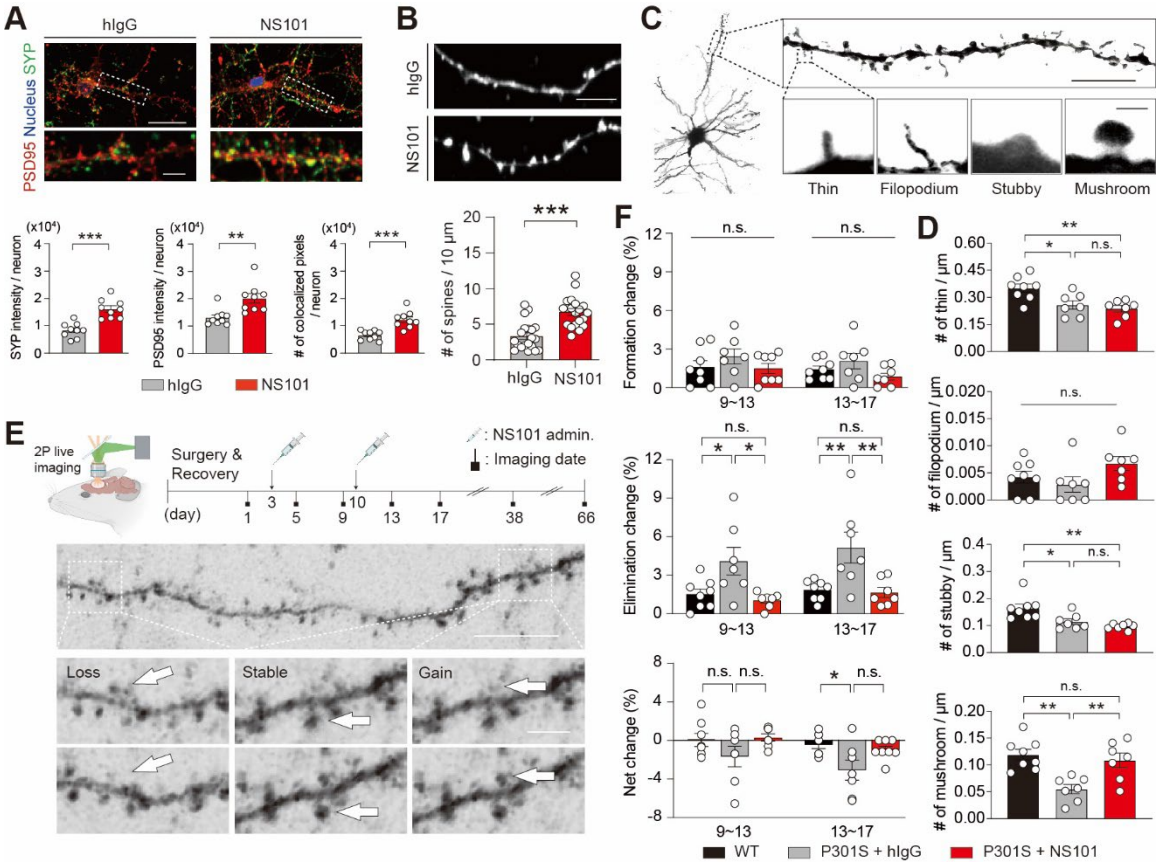

Figure 4. NS101 prevents synapse elimination, increasing functional synapses in AD model.

(A) Representative ICC image of neurons treated with hIgG or NS101. Cells were stained with SYP (green), PSD95 (red), and nucleus (blue) for quantification (n = 9 per group). Scale bar, 20 μm. (B) Representative image of dendritic spines of hippocampal neurons after DiI membrane staining and quantification of the number of spines (n = 20 per group). Scale bar, 5 μm. (C) Representative Golgi staining image of a cortical neuron in the P301S mouse brain for spine classification. Scale bar, 10 μm (dendrite), 1 μm (spine). (D) Quantification of the number of different types of spines before and after NS101 treatment (n = 8 to 7 per group). (E) Representative image of spine dynamics in the P301S mouse brain. After cranial window surgery, dendritic spines in the somatosensory cortex were measured at respective time points. Scale bar, 10 μm (dendrite), 1 μm (spine). (F) Quantification of spine dynamics at days 9~13 and 13~17 in P301S mice. Formation and elimination rate, and their net changes after intraperitoneal administration of 30 mg/kg NS101 (n = 7 to 8 per group). Data are presented as the mean ± SEM. Unpaired t-test in (A) and (B), one-way ANOVA followed by Tukey's multiple comparison test in (D), and one-way ANOVA with Bonferroni's multiple comparisons test in (F) were used to calculate *P* values. n.s., not significant; *$P < 0.05$, **$P < 0.01$, ***$P < 0.001$.

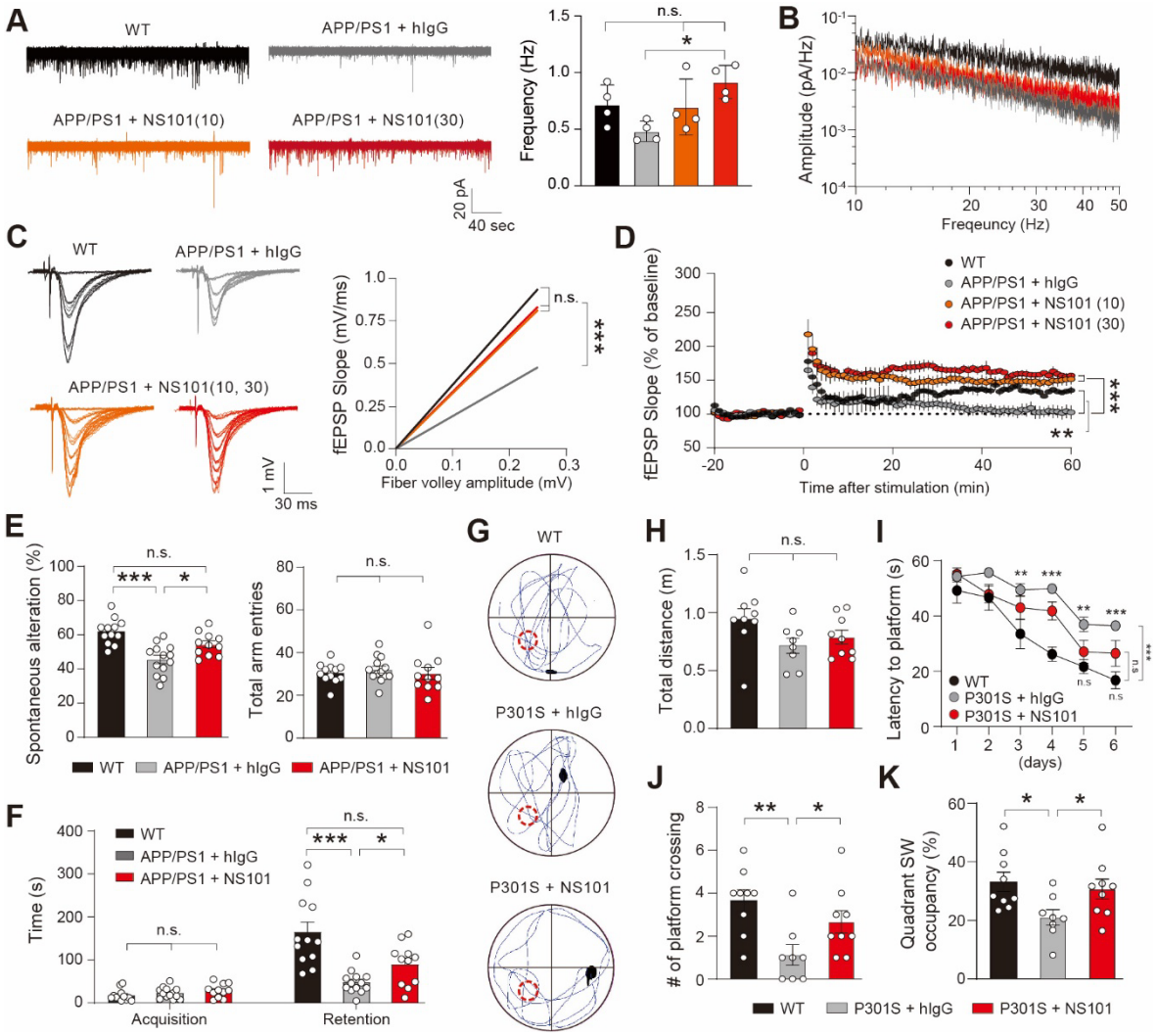

Figure 5. NS101 restores synaptic activity and cognitive behavior in AD.

(A) Representative mEPSC traces in hippocampal CA1 neurons of APP/PS1 mice and their frequency quantification (n = 4 per group). (B) Power spectrum analysis, displaying the averaged line of the dominating spikes before and after NS101 administration. (C) Representative input-output traces and fEPSP slopes plotted against fiber volley amplitudes in hippocampal CA1 neurons of WT and APP/PS1 mice treated with either hIgG or 10 mg/kg and 30 mg/kg NS101 (n = 5 per group). (D) The averaged fEPSP amplitude before and after theta burst stimulation to Schaffer collaterals for LTP induction (n = 5 to 6 per group). (E) Quantification of short-term memory in APP/PS1 mice using the Y-maze task (n = 11 to 13 per group). (F) Quantification of long-term memory in APP/PS1 mice using the passive avoidance task (n = 11 to 13 per group). Quantification of spatial learning and memory evaluated via the Morris water maze, (G) swimming trajectory of WT and P301S nice, (H) total distance, (I) latency to the platform, (J) the number of platform crossings, and (K) quadrant occupancy (n = 9 to 12 per group). Data are presented as the mean ± SEM. One-way ANOVA followed by Tukey's multiple comparison test in (A, C, D, E, F, H, J, and K) and two-way ANOVA (for I) followed by Newman-Keuls multiple comparisons test in (I) were used to calculate *P* values. n.s., not significant; **P* < 0.05, ***P* < 0.01, ****P* < 0.001.

Supplementary Materials for

The antibody NS101 restores synapse and cognition in Alzheimer's disease.

Authors: Han-Byul Kim[1†], Sangjin Yoo[1†], Hoyun Kwak[1†], Shi-Xun Ma[1†], Ryunhee Kim[1], Minhyeok Lee[1], Nui Ha[1], Soonil Pyo[1], Soon-Gu Kwon[1], Eun-Ho Cho[1], Sang-Myeong Lee[1], Juwon Jang[1], Wonkyum Kim[1], Hae-Chul Park[2], Minkyung Baek[3], Yosub Park[1], Ji-Young Park[5], Jin-Woo Park[6, 7], Sun Wook Hwang[4], Jong-Ik Hwang[4], Jae Young Seong[1, 4, *]

Corresponding author: jyseong@korea.ac.kr

List of Supplementary Materials

Figs. S1 to S6
Tables S1 to S5

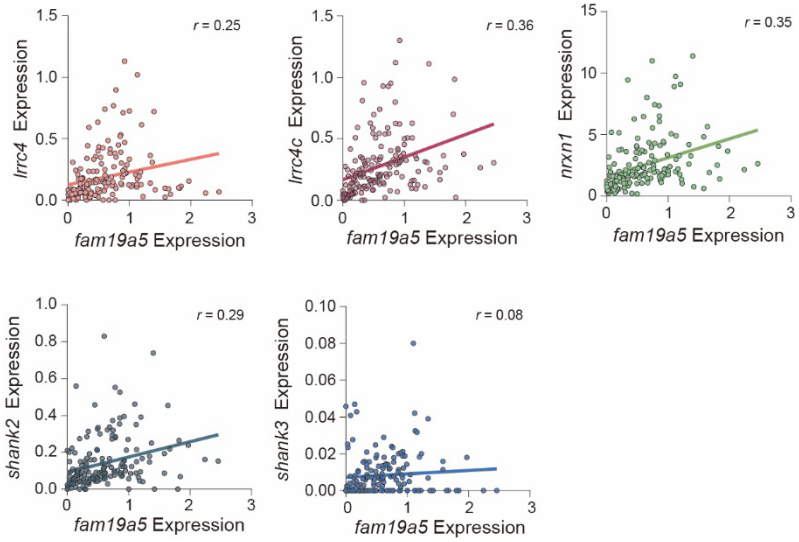

Fig. S1. FAM19A5 interacts with LRRC4B.

Correlation of RNA transcript levels between *fam19a5* and other synaptic adhesion molecules (*lrrc4*, *lrrc4c*, *nrxn1*, *shank2*, *shank3*) from 168 neuron types. Correlation coefficient; *r*.

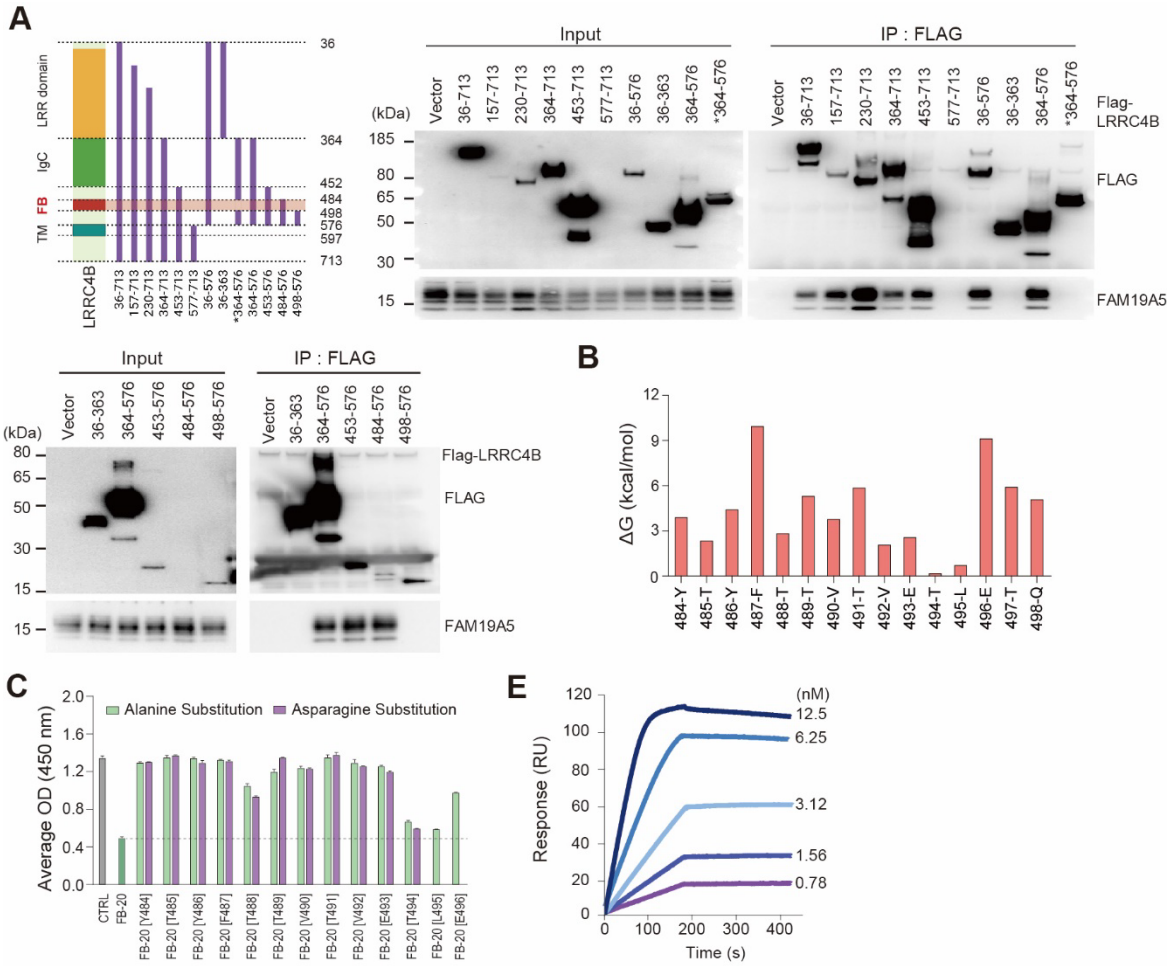

D Amino acid - position / ΔG (kcal/mol)

THR-44	CYS-45	GLU-46	ILE-47	VAL-48	THR-49	LEU-50	ASP-51	ARG-52	ASP-53	SER-54
0.01	0.14	-0.55	-0.12	0.3	0.25	0.3	-1.26	13.38	-1.6	0.29
SER-55	GLN-56	PRO-57	**ARG-58**	**ARG-59**	THR-60	ILE-61	ARG-63	GLN-64	THR-65	ARG-67
0.21	4.21	0.63	**2.84**	**5.33**	9.39	6.04	2.14	5.34	2.8	1.07
CYS-68	CYS-70	ARG-71	LYS-72	GLY-73	GLN-74	ILE-75	GLY-77	THR-78	THR-79	ARG-80
-0.75	-1.82	0.58	0.37	-0.02	0.06	0.13	-0.88	1.24	0.44	1.96
ARG-82	PRO-83	CYS-85	VAL-86	ASP-87	ARG-89	ILE-90	ILE-91	LYS-92	THR-93	LYS-94
1.14	0.63	0.34	-0.28	-0.81	0.64	-0.01	-0.15	0.49	-0.01	0.69
GLN-95	TRP-96	CYS-97	ASP-98	MET-99	LEU-100	PRO-101	CYS-102	LEU-103	GLU-104	GLY-105
0.01	-0.26	0.14	-0.98	-0.06	-0.2	-1.71	1.72	-1.37	-1.73	0
GLU-106	GLY-107	CYS-108	ASP-109	LEU-110	LEU-111	ILE-112	ASN-113	ARG-114	SER-115	GLY-116
-5.14	0.08	-0.47	-1.51	-0.2	-0.24	-0.02	-0.06	0.82	0.02	-0.14
TRP-117	THR-118	CYS-119	THR-120	GLN-121	PRO-122	GLY-123	GLY-124	**ARG-125**	ILE-126	**LYS-127**
-1.3	0	0.13	0.13	3.26	0.23	-0.28	0.02	20.06	0.55	13.12
THR-128	THR-129	THR-130	VAL-131	SER-132						
0.7	2.13	0.34	0.47	-0.58						

F

```
                                                                  FB domain
                                460       470       480       490       500       510       520       530       540
Hu-LRRC4B   LNVSAVDPVA AGGTGSGGGG PGGSGGVGGG SGGYTYFTTV TVETLETQPG EEALQPRGTE KEPPGPTTDG VWGGGRPGDA AGPASSSTTA
Ms-LRRC4B   SATLNVSAVD PVAAGGPGGG GPGGGGGAGG AGGYTYFTTV TVETLETQPG EEAQQPRGTE KEPPGPTTDG AWGGGRPDAA APASASTTAP
Rt-LRRC4B   SATLNVSAVD PVAAGGPGGG GPGGGGGAGG AGGYTYFTTV TVETLETQPG EEAQQPRGTE KEPPGPTTDG AWGGGRPDAA APASASTTAP
Mk-LRRC4B   AVDPVAAGGG GPGGGSGGPG GSGGSPGGGG GGGYTYFTTV TVETLETQPG EETLQPRGTE KEPPGPTTDG VWGGGRPGDA AGPASSSTTA
Dg-LRRC4B   LNVSAVDPVA AGGTGGGGGG PGGGGGVGGG SGGYTYFTTV TVETLETQPG EEALQPRGTE KEPPGPTTDG VWGGGRPGDA AGPASSSTTA
Zf-LRRC4B   QDTGPYTCMV TNSAGNTTAT AVLNVSAPDP GNGYSYFTTV TVETVETGQE GHDSPARQFV NETFISFPGP TAASTSAGPT GSMLSSLSPR
```

Fig. S2. Screening of LRRC4B and FAM19A5 to identify their binding sites.

(A) Domain architecture of LRRC4B deletion constructs (left) and co-IP and counterpart co-IP of LRRC4B deletion constructs (right). (B) Predicted binding free energy of the LRRC4B FB region with Ala substitution mutations for each residue. All residues in the FB protein were critical to binding except T494 and L495. (C) The key residues for FAM19A5-LRRC4B were confirmed via ELISA using the mutated FB proteins (captured by LRRC4B(36-576)-hFc, detected by HRP-conjugated C-A5-Ab). (D) The predicted binding free energy of FAM19A5 after Ala scanning. Competitive binding sites for the FB domain and NS101 (orange) and key residues for binding (pink) are highlighted. (E) SPR measurement to determine the binding affinity between LRRC4B and FAM19A5. Signals were collected from a chip coated with FB-containing protein (LRRC4B(453-576)-hFc) while treating FAM19A5 in a dose-dependent manner (0.78~12.5 nM, $K_a = 4.892 \times 10^6\ M^{-1}\ s^{-1}$, $K_d = 1.570 \times 10^{-4}\ s^{-1}$, $K_D = 3.209 \times 10^{-11}$ M). (F) Sequence alignment of LRRC4B FB sequences across species, including humans.

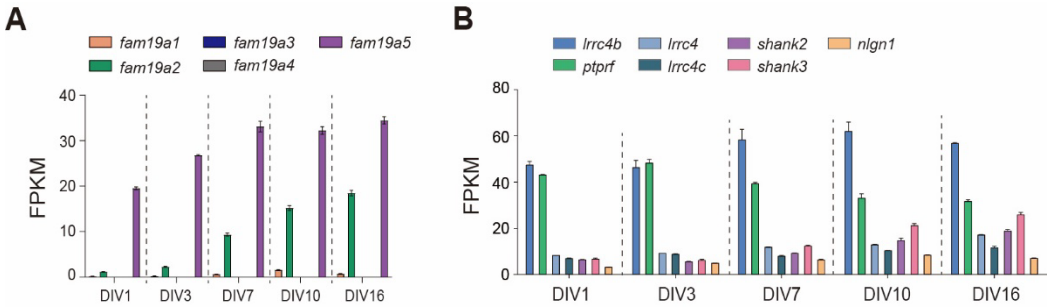

Fig. S3. RNA expression levels of the FAM19A family and synapse adhesion molecules.

RNA transcription levels of (A) the *fam19a* family and (B) synapse adhesion molecules in primary hippocampal neurons at the indicated time points (n = 3 per group).

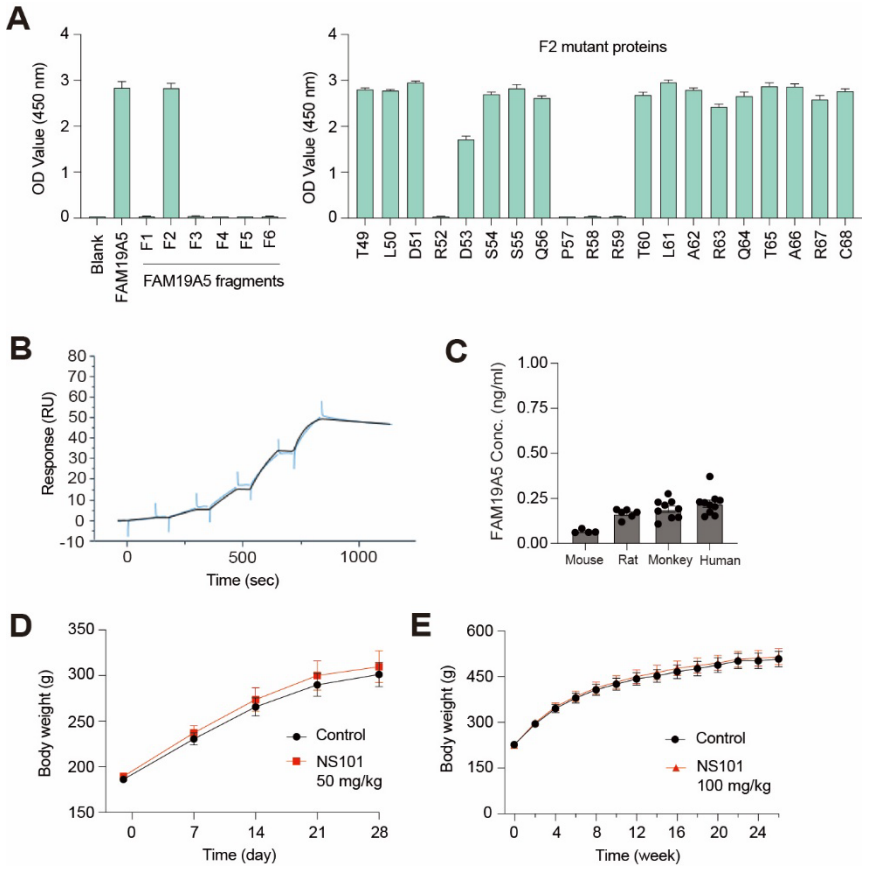

Fig. S4. Characterization of NS101.

(A) Epitope mapping of FAM19A5. Binding of NS101 to FAM19A5 and synthetic peptides (F1~F6 and F2 mutant peptides, see table S3 and S4) were evaluated via ELISA (captured by FAM19A5 fragment, bound by NS101, detected by HRP-conjugated hIgG). The amino acid residues are numbered according to the human FAM19A5 sequence. (B) SPR measurement to determine the binding affinity of NS101 to FAM19A5. Signals were collected from a chip coated with FAM19A5 while treating increasing concentrations of NS101 (0.12~10 nM, K_a = 2.11 x 10^6 M^{-1} s^{-1}, K_d = 2.34 x 10^{-4} s^{-1}, K_D = 1.11 x 10^{-10} M). (C) Quantification of the secreted FAM19A5 in the blood from mice, rats, monkeys, and humans via ELISA (captured by His-TEV hLRRC4B(453-576), detected by HRP-conjugated SS01) (n = 4 to 10 per group). (D-E) Rat body weight measurement with or without regular NS101 administration for (D) 4 weeks, weekly (n = 20 to 30 per group) or (E) 26 weeks, biweekly (n = 42 to 44 per group). Data are presented as the mean ± SEM. Two-way ANOVA followed by Sidak's multiple comparison test in (D) and (E) was used to calculate *P* values.

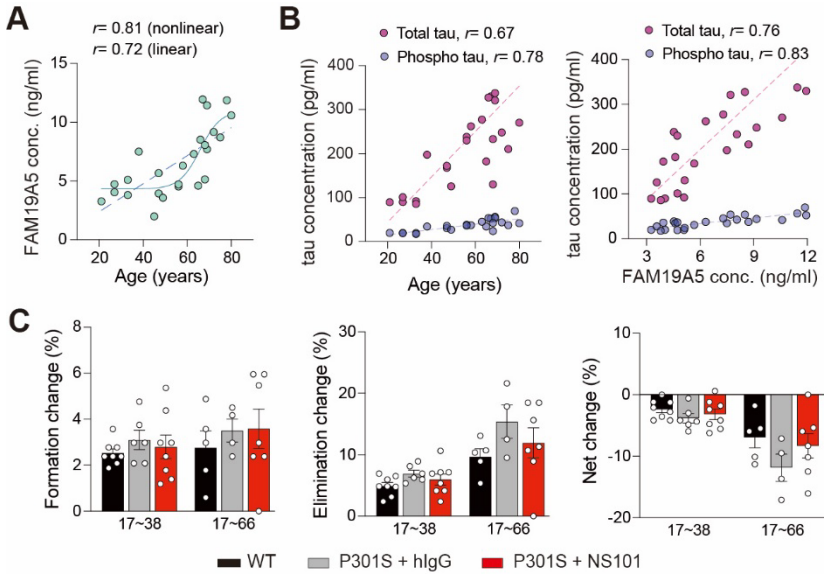

Fig. S5. Dendritic spine dynamics in the AD model before and after NS101.

(A) Correlation between FAM19A5 in human CSF and age. (B) Correlation of tau with age (left) and with FAM19A5 (right) in human CSF. Correlation coefficient; *r*. (C) Quantification of spine dynamics at day 17~38 and 17~66 in P301S mice. Formation and elimination rate, and their net changes after intraperitoneal administration of 30 mg/kg NS101 (n = 4 to 8 per group). Data are presented as the mean ± SEM. One-way ANOVA with Bonferroni's multiple comparisons test in (C) was used to calculate *P* values.

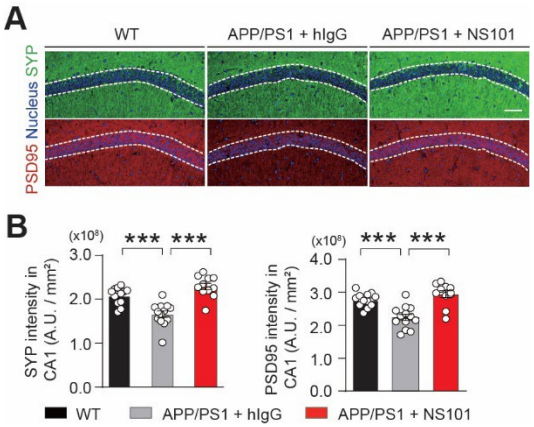

Fig. S6. Synapse was restored in the AD model after NS101.

(A) Representative IHC image of hippocampal CA1 in APP/PS1 mice after IV administration of NS101 or hIgG (30 mg/kg each) stained with SYP (green) and PSD95 (red). Scale bar, 100 µm. (B) Quantified intensity of synaptic marker proteins from (A) (n = 11 to 12 per group). Data are presented as the mean ± SEM. One-way ANOVA with Tukey's multiple comparisons test in (B) was used to calculate *P* values. ***$P < 0.001$.

Table S1. Primers for cloning.

Insert	Primer Sequence	
LRRC4B 36-713	For	GATGACGACAAGCTTGCCGGTGGAGGTGGAG
	Rev	GTTTTTGTTCGGATCCTCAGATCTGCGTCTCTTGC
LRRC4B 157-713	For	GATGACGACAAGCTTCTGTCCAAGCTGCGGG
	Rev	GTTTTTGTTCGGATCCTCAGATCTGCGTCTCTTGC
LRRC4B 230-713	For	GATGACGACAAGCTTCGCCTGGAGGAGCTGG
	Rev	GTTTTTGTTCGGATCCTCAGATCTGCGTCTCTTGC
LRRC4B 364-713	For	GATGACGACAAGCTTCCCGTCATCGTGGAGC
	Rev	GTTTTTGTTCGGATCCTCAGATCTGCGTCTCTTGC
LRRC4B 453-713	For	GATGACGACAAGCTTGTCTCGGCCGTGGACC
	Rev	GTTTTTGTTCGGATCCTCAGATCTGCGTCTCTTGC
LRRC4B 577-713	For	GATGACGACAAGCTTATCATCATCGGCTGCTTC
	Rev	GTTTTTGTTCGGATCCTCAGATCTGCGTCTCTTGC
LRRC4B 36-576	For	GATGACGACAAGCTTGCCGGTGGAGGTGGAG
	Rev	GTTTTTGTTCGGATCCTCATTTGGTGGTCTTCATG
LRRC4B 36-363	For	GATGACGACAAGCTTGCCGGTGGAGGTGGAG
	Rev	GTTTTTGTTCGGATCCTCACGCATAGCAGGTG
LRRC4B 364-576	For	GATGACGACAAGCTTCCCGTCATCGTGGAGC
	Rev	GTTTTTGTTCGGATCCTCATTTGGTGGTCTTCATG
LRRC4B D364-576	For	GATGACGACAAGCTTGCCGGTGGAGGTGGAG
	InRev	GAAGCAGCCGATGATGATCGCATAGCAGGTGAAATG
	InFor	CATTTCACCTGCTATGCGATCATCATCGGCTGCTTC
	Rev	GTTTTTGTTCGGATCCTCAGATCTGCGTCTCTTGC
LRRC4B 453-576	For	GATGACGACAAGCTTGTCTCGGCCGTGGACC
	Rev	GTTTTTGTTCGGATCCTCATTTGGTGGTCTTCATG
LRRC4B 484-576	For	GATGACGACAAGCTTTACACCTACTTCACCACGGTG
	Rev	GTTTTTGTTCGGATCCTCATTTGGTGGTCTTCATG
LRRC4B 498-576	For	GATGACGACAAGCTTCAGCCCGGAGAGGAGG
	Rev	GTTTTTGTTCGGATCCTCATTTGGTGGTCTTCATG
LRRC4C 354-527	For	GATGACGACAAGCTTCCGGTGATTGTGGAGCC
	Rev	GTTTTTGTTCGGATCCTCATTTGGTAGTCTTCATGACC
LRRC4 353-527	For	GATGACGACAAGCTTCCCTTCATCATGGACGC
	Rev	GTTTTTGTTCGGATCCTCACTTGGTGGTCTTCATGAC
LRRC4B 453-576 (T488A, T489A)	For	GATGACGACAAGCTTGTCTCGGCCGTGGACC
	InRev	CACGGTCACGGCCGCGAAGTAGGTGTAG
	InFor	CTTCGCGGCCGTGACCGTGGAGAC
	Rev	GTTTTTGTTCGGATCCTCATTTGGTGGTCTTCATG
LRRC4B 453-576 (T488S, T489S)	For	GATGACGACAAGCTTGTCTCGGCCGTGGACC
	InRev1	GTCTCCACGGTCACAGACGAGAAGTAGGTGTAG
	InFor1	CTACACCTACTTCTCGTCTGTGACCGTGGAGAC
	InRev2	CAGACACCGTCAGACGAGGGCCCTG

	InFor2	CAGGGCCCTCGTCTGACGGTGTCTG
	Rev	GTTTTTGTTCGGATCCTCATTTGGTGGTCTTCATG
LRRC4B 36-713 (T488A, T489A)	For	GATGACGACAAGCTTGCCGGTGGAGGTGGAG
	InRev	CACGGTCACGGCCGCGAAGTAGGTGTAG
	InFor	CTACACCTACTTCGCGGCCGTGACCGTG
	Rev	GTTTTTGTTCGGATCCTCAGATCTGCGTCTCTTGC
FAM19A5 (R58A, R59A)	For	CAGCCAGCCTGCCGCCACGATC
	InRev	GATCGTGGCGGCAGGCTGGCTG
	InFor	ATGGAGACAGACACACTCCTGCTATGGGTACTG
	Rev	CAGTACCCATAGCAGGAGTGTGTCTGTCTCCAT
FAM19A5 (R125A, K127A)	For	CGGGGCCATAGCCACCACCACGGTCTC
	InRev	GAACGAAATAGACAGATCGCTGAGATAGGTGCCTCAC
	InFor	GTGAGGCACCTATCTCAGCGATCTGTCTATTTCGTTC
	Rev	GAGACCGTGGTGGTGGCTATGGCCCCG
PTPRF (30-1263)	For	GTTCCACTGGTGACAAGCTTGACAGCAAACCTGTC
	Rev	CCACCGCCGAATTCCCACAGCATCTCCGGC

Table S2. The sequences of point mutated FB-20 proteins

Name	Manufacturer	Lot No.	Amino acid sequence
FB-20	Anygen	K210024	GYTYFTTVTVETLETQPGEE
FB-20[Y484A]	Anygen	K210410	G**A**TYFTTVTVETLETQPGEE
FB-20[Y485A]	Anygen	K210411	GY**A**YFTTVTVETLETQPGEE
FB-20[Y486A]	Anygen	K210412	GYT**A**FTTVTVETLETQPGEE
FB-20[Y487A]	Anygen	K210413	GYTY**A**TTVTVETLETQPGEE
FB-20[Y488A]	Anygen	K210414	GYTYF**A**TVTVETLETQPGEE
FB-20[Y489A]	Anygen	K210415	GYTYFT**A**VTVETLETQPGEE
FB-20[Y490A]	Anygen	K210416	GYTYFTT**A**TVETLETQPGEE
FB-20[Y491A]	Anygen	K210417	GYTYFTTV**A**VETLETQPGEE
FB-20[Y492A]	Anygen	K210418	GYTYFTTVT**A**ETLETQPGEE
FB-20[Y493A]	Anygen	K210419	GYTYFTTVTV**A**TLETQPGEE
FB-20[Y494A]	Anygen	K210420	GYTYFTTVTVE**A**LETQPGEE
FB-20[Y495A]	Anygen	K210421	GYTYFTTVTVET**A**ETQPGEE
FB-20[Y496A]	Anygen	K210422	GYTYFTTVTVETL**A**TQPGEE
FB-20[Y484N]	Anygen	K210423	G**N**TYFTTVTVETLETQPGEE
FB-20[Y485N]	Anygen	K210424	GY**N**YFTTVTVETLETQPGEE
FB-20[Y486N]	Anygen	K210425	GYT**N**FTTVTVETLETQPGEE
FB-20[Y487N]	Anygen	K210426	GYTY**N**TTVTVETLETQPGEE
FB-20[Y488N]	Anygen	K210427	GYTYF**N**TVTVETLETQPGEE
FB-20[Y489N]	Anygen	K210428	GYTYFT**N**VTVETLETQPGEE
FB-20[Y490N]	Anygen	K210429	GYTYFTT**N**TVETLETQPGEE

FB-20[Y491N]	Anygen	K210430	GYTYFTTVNVETLETQPGEE
FB-20[Y492N]	Anygen	K210431	GYTYFTTVTNETLETQPGEE
FB-20[Y493N]	Anygen	K210432	GYTYFTTVTVNTLETQPGEE
FB-20[Y494N]	Anygen	K210433	GYTYFTTVTVENLETQPGEE

Table S3. The sequences of FAM19A5 fragment proteins

Name	Manufacturer	Lot No.	Amino acid sequence (C → S)
F1	Peptron	15-103901	QFLKEGQLAAGTSEIVTLDR-GGGSC-BSA
F2	Peptron	15-103902	TLDRDSSQPRRTIARQTARS-GGGSC-BSA
F3	Peptron	15-103903	TARSASRKGQIAGTTRARPA-GGGSC-BSA
F4	Peptron	15-103904	ARPASVDARIIKTKQWSDML-GGGSC-BSA
F5	Peptron	15-103905	SDMLPSLEGEGSDLLINRSG-GGGSC-BSA
F6	Peptron	15-103906	NRSGWTSTQPGGRIKTTTVS-GGGSC-BSA

Table S4. The sequences of point mutated F2 fragments of FAM19A5

Name	Manufacturer	Lot No.	Amino acid sequence
F2-01	Peptron	16-105901	TADRDSSQPRRTIARQTARC-BSA
F2-02	Peptron	16-105902	TLARDSSQPRRTIARQTARC-BSA
F2-03	Peptron	16-105903	TLDRASSQPRRTIARQTARC-BSA
F2-04	Peptron	16-105904	TLDRDASQPRRTIARQTARC-BSA
F2-05	Peptron	16-105905	TLDRDSAQPRRTIARQTARC-BSA
F2-06	Peptron	16-105906	TLDRDSSAPRRTIARQTARC-BSA
F2-07	Peptron	16-105907	TLDRDSSQARRTIARQTARC-BSA
F2-08	Peptron	16-105908	TLDRDSSQPRATIARQTARC-BSA
F2-09	Peptron	16-105909	TLDRDSSQPRRAIARQTARC-BSA
F2-10	Peptron	16-105910	TLDRDSSQPRRTAARQTARC-BSA
F2-11	Peptron	16-105911	TLDRDSSQPRRTIRRQTARC-BSA
F2-12	Peptron	16-105912	TLDRDSSQPRRTIAAQTARC-BSA
F2-13	Peptron	16-105913	TLDRDSSQPRRTIARQTVRC-BSA
F2-14	Peptron	17-99901	ALDRDSSQPRRTIARQTARC-BSA
F2-15	Peptron	17-99902	TLDADSSQPRRTIARQTARC-BSA
F2-16	Peptron	17-99903	TLDRDSSQPARTIARQTARC-BSA
F2-17	Peptron	17-99904	TLDRDSSQPRRTIARATARC-BSA
F2-18	Peptron	17-99905	TLDRDSSQPRRTIARQAARC-BSA
F2-19	Peptron	17-99906	TLDRDSSQPRRTIARQTAAC-BSA

F2-20	Peptron	17-99907	TLDRDSSQPRRTIARQTARA-GGGSC-BSA

Table S5. The antibodies used in this study.

Mouse monoclonal anti-Synaptophysin	Sigma-Aldrich	Cat# S5768
Mouse monoclonal anti-PSD95	Invitrogen	Cat# MA1-045
Mouse monoclonal anti-Tau5	Invitrogen	Cat# AHB0042
Mouse monoclonal anti-NGL-3/LRRC4B	R&D Systems	Cat# MAB69191
Mouse monoclonal anti-FLAG M2	Sigma-Aldrich	Cat# F1804
Mouse monoclonal anti-V5	Invitrogen	Cat# R960CUS
Donkey anti-Human IgG-HRP	Jackson ImmunoResearch	Cat# 715-035-149
Donkey anti-Mouse IgG-HRP	Jackson ImmunoResearch	Cat# 715-035-150
Donkey anti-Human IgG-Cy3	Jackson ImmunoResearch	Cat# 709-165-149
Rabbit anti-Human IgG Heavy chain	Invitrogen	Cat# SA5-10223
Rabbit anti-Human IgG Fc-HRP	Invitrogen	Cat# 31423
Goat anti-Human kappa light chain-HRP	Invitrogen	Cat# A18853
anti-Human isotype control	Invitrogen	Cat# 31154
Anti-Human IgG1, kappa isotype control	Sino Biological	Cat# HG1K